Particle-balance models for pulsed sputtering magnetrons

Chunqing Huo,[1,2,3] D. Lundin,[4,*] J. T. Gudmundsson,[1,4,5,†]
M. A. Raadu,[1] J. W. Bradley,[6] and N. Brenning[1,7,‡]

[1]*Department of Space and Plasma Physics, School of Electrical Engineering, KTH–Royal Institute of Technology, SE-100 44, Stockholm, Sweden*

[2]*Shenzhen Key Laboratory of Special Functional Materials, Shenzhen Engineering Laboratory for Advanced Technology of Ceramics, College of Materials Science and Engineering, Shenzhen University, Shenzhen 518060, China*

[3]*Key Laboratory of Optoelectronic Devices and Systems of Ministry of Education and Guangdong Province, College of Optoelectronic Engineering, Shenzhen University, Shenzhen 518060, China*

[4]*Laboratoire de Physique des Gaz et Plasmas - LPGP, UMR 8578 CNRS, Université Paris–Sud, Université Paris–Saclay, 91405 Orsay Cedex, France*

[5]*Science Institute, University of Iceland, Dunhaga 3, IS-107 Reykjavik, Iceland*

[6]*Department of Electrical Engineering and Electronics, University of Liverpool, Brownlow Hill, Liverpool, L69 3GJ, UK*

[7]*Plasma and Coatings Physics Division, IFM-Materials Physics, Linköping University, SE-581 83, Linköping, Sweden*

(Dated: May 3, 2017)

Abstract

The time-dependent plasma discharge ionization region model (IRM) has been under continuous development during the past seven years and used in several studies of the ionization region of high-power impulse magnetron sputtering (HiPIMS) discharges. In the present work, a complete description of the most recent version of the IRM is given, which includes improvements, such as allowing for returning of the working gas atoms from the target, a separate treatment of hot secondary electrons, addition of doubly charged metal ions, etc. To show the general applicability of the IRM, two different HiPIMS discharges are investigated. The first set concerns 400 μs long discharge pulses applied to an Al target in an Ar atmosphere at 1.8 Pa. The second set focuses on 100 μs long discharge pulses applied to a Ti target in an Ar atmosphere at 0.54 Pa, and explorers the effects when varying the magnetic field strength. The model results show that Al^{2+}-ions contribute negligibly to the production of secondary electrons, while Ti^{2+}-ions effectively contribute to the production of secondary electrons. Similarly, the model results show that for an argon discharge with Al target the contribution of Al^{+}-ions to the discharge current is over 90 % at 800 V, while Al^{+}-ions and Ar^{+}-ions contribute roughly equally to the discharge current at 400 V. For high currents the discharge with Al target develops almost pure self-sputter recycling, while the discharge with Ti target exhibits close to a 50/50 combination of self-sputter recycling and working gas-recycling. For a Ti target, a self-sputter yield significantly below unity makes working gas-recycling necessary at high currents. In the discharge with Ti target the **B**-field was reduced in steps from the nominal value, which resulted in a corresponding stepwise increase in the discharge resistivity.

*daniel.lundin@u-psud.fr

†tumi@hi.is

‡nils.brenning@ee.kth.se

I. INTRODUCTION

Magnetron sputtering is a widely used tool that has been applied successfully by various industries for deposition of thin films and coatings for over four decades. The high power impulse magnetron sputtering (HiPIMS) discharge is an extension of this technique that provides ionized physical vapor deposition (IPVD) and has attracted much interest lately [1–3]. In HiPIMS, high power is applied to the magnetron target (cathode) in unipolar pulses at low duty cycle, while keeping the average power about two orders of magnitude lower than the peak power [2]. This results in a high plasma density (electron density) and a high ionization fraction of the deposited material. The high ionization fraction has opened up new ways to engineer thin films with improved properties, since it allows for controlling the energy and direction of the deposition species [1, 3]. This is a significant advantage over conventional dc magnetron sputtering (dcMS), where the sputtered material consists mainly of neutral species [1].

The ionization region model (IRM), introduced by Raadu et al. [4], is a flexible modeling tool for studying the plasma behavior during a HiPIMS pulse and the afterglow. The IRM is a zero-dimensional, time-dependent plasma chemical model of the ionization region (IR). The IR is located in close vicinity of the target race track and observed as a dense, brightly glowing plasma, as demonstrated in Figure 1. The model has so far been applied to study gas rarefaction and refill processes [4, 5] the loss in deposition rate [6], the electron heating mechanism [7] and the onset of self-sputtering [8] in an argon HiPIMS discharge with Al target. For an argon discharge with Ti target, the temporal behavior of the argon metastable state has been investigated and compared to experiments [9], along with exploring its role and importance in the ionization processes in HiPIMS [10]. More recently, the IRM has been extended to model a reactive Ar/O_2 HiPIMS discharge with Ti target by adding a reaction set for oxygen to the discharge model as well as adding the resulting extra oxygen-related surface processes [11, 12]. The IRM has also been adapted and applied to explore other types of discharges, such as the hollow cathode [13].

The development of the IRM and the various versions used in earlier publications [4–8] are reviewed and compared by Huo [15]. The purpose of the present work is to provide a complete and up to date description of the IRM in order for other researchers to develop their own versions, and continue the work on improving the understanding of the HiPIMS

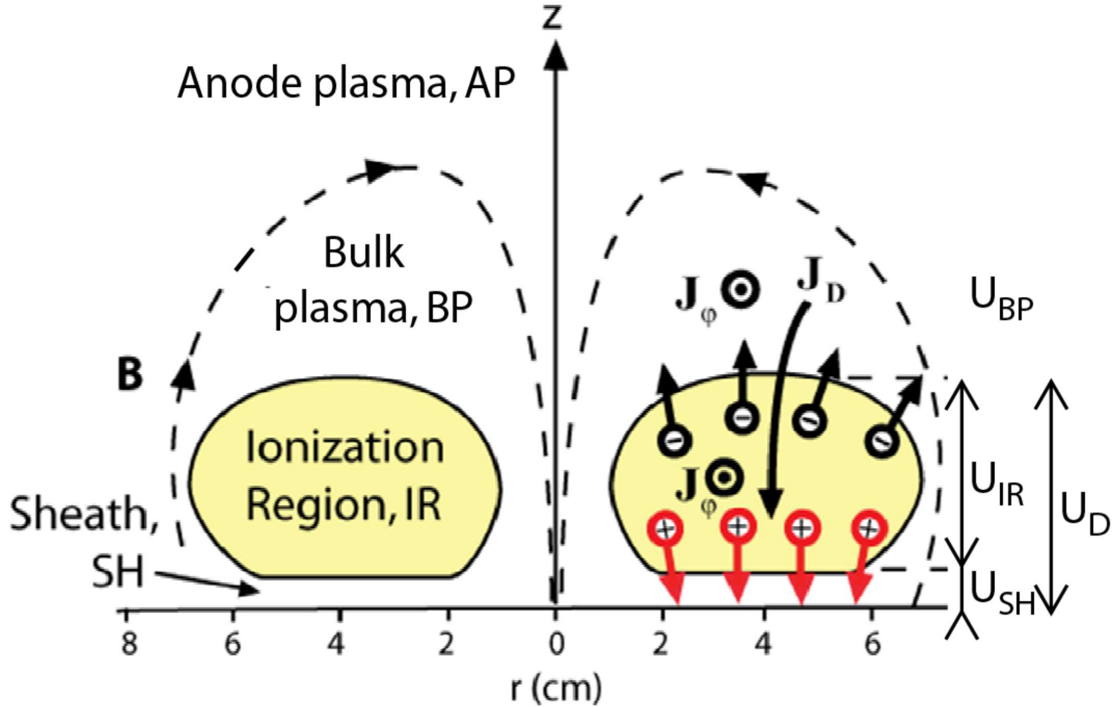

FIG. 1: A separation of the sputtering magnetron discharge into regions based on the dominating physics. The sheath (SH) is defined by a substantial charge imbalance such that $(n_\mathrm{i} - n_\mathrm{e})/n_\mathrm{e} \geq 1$. The ionization region (IR) is where most of the ionization occurs. In the bulk plasma (BP), cross-$\mathbf{B}$ current transport of electrons from the IR to the anode plasma is the key process. In the anode plasma (AP) finally, the discharge current can close along the magnetic field to the anode and/or to the walls of the device [14]. The IR can be approximately identified with the extended presheath although, also in the BP, the need for cross-$\mathbf{B}$ electron transport can sustain an electric field. From Huo et al. [5].

discharge as well as other types of materials processing plasma discharges. To this purpose we here give explicit equations and reaction data sets for the most recent version of the IRM, exemplify the types of results that can be obtained, and discuss the reliability of the model output. Furthermore, to show the general applicability of the IRM, we have applied the IRM to two series of HiPIMS experiments performed at the Lawrence Berkeley National Laboratory and the University of Liverpool, respectively. The former study uses an Al target and includes current densities at the cathode up to 3.75 A cm^{-2}, i.e. in a range where the self-sputtering mode is important [16], while the latter study uses a Ti target and focuses on the effect of varying the magnetic field strength in the magnetron target vicinity [17].

The paper is organized as follows. Section II gives a detailed description of the IRM where section II A discusses the terms that are included in the particle balance equations for

each particle and section II B discusses the power balance equations and the terms that are included in the power balance equations. The plasma chemistry including the reaction set and rate coefficients used in the model are discussed in section III. Section IV introduces the experimental data we explore here. Section V describes the fitting of the model to the experimental data and the sensitivity analysis performed for each data set. Section VI includes the model results and a discussion including comparison of a discharge with aluminum target and with titanium target as well as the effect of magnetic field strength. Section VII finally gives a summary of the main findings.

II. THE IONIZATION REGION MODEL

Using the IRM the time evolution of neutral and charged species and the electron temperature in sputtering magnetron discharges can be calculated and explored further. The model is based on a separation of the discharge volume into separate regions defined by the dominating physics, as detailed in the caption of Figure 1. The model is limited to the ionization region (IR), which, in the IRM, is defined as an annular cylinder with outer radii r_{c2}, and inner radii r_{c1} marking the race track region, and length $L = z_2 - z_1$, extending from z_1 to z_2 axially away from the target. This is a volume averaged global model of the plasma chemistry and the model assumes only volume-averaged values over the whole IR volume for the electron, ion and neutral densities and the electron temperature. Geometrical effects are included indirectly as loss and gain rates across the boundaries of this annular cylinder to the target and the bulk plasma [4]. The temporal development is defined by a set of ordinary differential equations giving the first time derivatives of the electron energy and the particle densities for all the heavy particles. The electron density is found assuming quasi-neutrality of the plasma.

The model is constrained by experimental data input in the sense that it first needs to be adapted to an existing discharge (the geometry and the pressure, the process gas and target species, and a reaction set for these species), and then fitted to reproduce measured discharge current and voltage curves, $I_D(t)$ and $U_D(t)$, respectively. The fitting parameters are quantities for which accurate modeling is still beyond the range of what can be achieved. Much of the early IRM model development was based on discharges with Al target [5, 6], and for these two such model fitting parameters were found to be sufficient. One of these,

$U_{\rm IR}$ in the present IRM version, accounts for the power input to the electrons, and the other, β, accounts for the probability of back-attraction of ions to the target. The basic reason why these two quantities are so difficult to model is that they both depend on the rapidly varying, time- and space-dependent, electric forces acting on the charged particles within the spoke structures that are known to spontaneously arise in magnetron discharges [18–21]. As the IRM is a volume averaged model and densities are averaged over the azimuthal direction and thus spatial variations in particle density and potentials (potential humps), that are associated with these spokes, are averaged out. Thus the results of the IRM should be taken as representing more of qualitative trends than giving quantitative values. Besides $U_{\rm IR}$ and β, recent IRM-modeling with other target materials [11] has revealed that sometimes a third fitting parameter needs to be added to the list: the probability r of back-attraction of secondary-emitted electrons from the target. Also this parameter is extremely difficult to predict theoretically [22–24]. In the two discharges studied here the Al target needs only two fitting parameters, while the Ti target needs three. The analysis below will show the reason for this difference. The fitting process and the fitting parameters are further discussed in detail in section V. Some of the key variables in the model are listed in table I.

A. Particle balance

The species assumed in the IRM are electrons, ground state argon atoms Ar, hot argon atoms in the ground state $\rm Ar^H$, warm argon atoms in the ground state $\rm Ar^W$, metastable argon atoms $\rm Ar^m$, argon ions $\rm Ar^+$, metal neutrals M, singly ionized metal ions $\rm M^+$ and doubly ionized metal ions $\rm M^{2+}$. Collectively the electrons are denoted by e, the neutral gas species are denoted by g, and the ions are denoted by i. The species considered in the model are listed in table II. In generalized form, the particle balance equation for species X is given by

$$\frac{{\rm d}n^{(X)}}{{\rm d}t} = \sum_i R^{(X)}_{{\rm Generation},i} - \sum_j R^{(X)}_{{\rm Loss},j} \quad (1)$$

The two terms, $R_{{\rm Generation},i}$ and $R_{{\rm Loss},j}$, respectively, are the reaction rates of the various generation and loss processes that are related to the plasma chemistry in the IR of species X. The reaction rate R_j for a given reaction j in the volume is calculated as the product of

TABLE I: Variables that appear in the model.

Variable	Physics	Comment
r_{c1}, r_{c2}	The radial extent of the ionization region.	Estimated from light emission and race-track erosion
z_1, z_2	The axial extent of the ionization region.	Child sheath gives $z_1 \approx 0.2$ mm. z_2 is variable, estimated from the light emission.
β_{Ar^+}, β_{M^+}	The back-attraction probability of ions.	β is used as a current fitting parameter.
$\beta_{\mathrm{M}^{2+}}$,	The back-attraction probability of M^{2+}-ions.	
ξ_{pulse}	The fraction of the recombined Ar^+-ions at the target that is assumed to return during the pulse as Ar^{H} or Ar^{W}.	An important parameter for the Ar gas recycling process [5]
ξ_{H}	The fraction of ξ_{pulse} that is assumed to return as hot Ar^{H} atoms.	Hot Ar^{H} atoms are those ions that are reflected immediately with high energy. The other ions recombine and leave the surface as Ar^{W} at the target temperature.
F_{recycle}	A parameter for the gas recycling process.	See section V A for definition.
r	The recapture probability of secondary emitted electrons.	Sometimes needed as a third fitting parameter. Here taken to be in the range $0.25 < r < 1$.
m	A factor that accounts for secondary electrons ionizing in the sheath.	Here taken to be $m = 1$, corresponding to zero ionization in the sheath.
ϵ_{e}	The fraction of the electron energy that is used for ionization before being lost from the discharge process.	
γ_{Ar^+}	The secondary electron emission for argon ions	
$\gamma_{\mathrm{M}^{2+}}$	The secondary electron emission for doubly ionized metal ions	
$\gamma_{\mathrm{Ar}^+,\mathrm{eff}}$	The effective secondary electron emission for argon ions $\gamma_{\mathrm{Ar}^+,\mathrm{eff}} = \gamma_{\mathrm{Ar}^+}(1-r)\epsilon_{\mathrm{e}} m$	
$\gamma_{\mathrm{M}^{2+},\mathrm{eff}}$	The effective secondary electron emission for doubly ionized metal ions $\gamma_{\mathrm{M}^{2+},\mathrm{eff}} = \gamma_{\mathrm{M}^+}(1-r)\epsilon_{\mathrm{e}} m$	
$\mathcal{E}_{\mathrm{htc}}$	The energy loss to the cold electron population when a hot electron ionizes.	$\mathcal{E}_{\mathrm{htc}} = 10$ eV is used as default value; not a sensitive parameter.
U_{IR}	The potential across the ionization region.	Used as a current fitting parameter. Also determines ion energies for ions from the IR to the sheath.
U_{SH}	Sheath potential $U_{\mathrm{SH}} = U_{\mathrm{D}} - U_{\mathrm{IR}}$.	Determines ion and electron energies after passing the sheath.
T_{eH}	The "temperature" of the hot electron component.	The hot electrons are ascribed an effective temperature proportional to the beam input energy eU_{SH}.
f	The fraction of the total discharge voltage across IR.	$f = U_{\mathrm{IR}}/U_{\mathrm{D}}$ and replaces U_{IR} as a current fitting parameter.

the densities of the reactants and the rate coefficient k_j of the reaction,

$$R_j = k_j \times \prod_i n_{\mathrm{reactant},i} \qquad [\mathrm{m^{-3}s^{-1}}] \tag{2}$$

where $n_{\mathrm{reactant},i}$ is the density of the i-th reactant. The reaction rates in Eq. (1) can also describe additional generation and loss processes due to sputtering $R_{\mathrm{n,sputt}}$, neutral flux diffusion $R_{\mathrm{n,diff}}$, gas refill $R_{\mathrm{g,refill}}$, gas kick-out $R_{\mathrm{g,kick-out}}$, ion loss out of the IR or to surfaces $R_{\mathrm{i,loss}}$, and return of recombined positive gas ions $R_{\mathrm{g,return}}$ from the target. Each term is discussed in detail in sections II A 1 – II A 3. Note that not all terms are applicable for all species.

TABLE II: The species considered in the model.

Species	Physics	Comment
e^{C}	cold electron	Bulk electrons assumed to have Maxwellian EEDF
e^{H}	hot electron	Hot population energized by secondary electrons emitted from the target
Ar	argon atom	Cold (thermal) argon atoms in the ground state
Ar^{H}	hot argon atom	Argon ions that after recombination return as atoms from the target with a few eV energy
Ar^{W}	warm argon atom	Argon ions that penetrate the target surface, displace atoms, and then slowly diffuse to the surface and escape as atoms at lower energy ≤ 0.1 eV (the target temperature) [25]
Ar^{m}	metastable argon atom	Cold (thermal) argon atoms in the metastable state
Al	aluminum atom	Sputtered particle
Al^{+}	singly ionized aluminum	Sputtered and ionized particle
Al^{2+}	doubly ionized aluminum	Sputtered and twice ionized particle
Ti	titanium atom	Sputtered particle
Ti^{+}	singly ionized titanium	Sputtered and ionized particle
Ti^{2+}	doubly ionized titanium	Sputtered and twice ionized particle

1. Neutral particle balance

The rate at which species are sputtered off the target (Al and Ti in the present work) is given by a generation term

$$R_{\mathrm{n,sputt}} = \frac{\sum_i \Gamma_i^{\mathrm{RT}} S_{\mathrm{RT}} Y_i(E_i)}{V_{\mathrm{IR}}} \tag{3}$$

where n stands for neutral atom sputtered off the target and i stands for the ion involved in the process, $\Gamma_i^{\rm RT}$ is the flux of ion i towards the target, $S_{\rm RT}$ is the area of the sputtered region (race track), $Y_{\rm i}(E_{\rm i})$ is the energy dependent sputter yield for ion i bombarding the target, and $V_{\rm IR}$ is the total volume of the IR. The sputter yields depend on the ion energies $E_{\rm i}$ which we take to be the discharge voltage $U_{\rm D}(t)$. Thus the sputter yield follows the discharge voltage waveform and is time dependent (see [26]). Here i = Ti^+, Ti^{2+}, Al^+, Al^{2+}, or Ar^+. In addition, neutral atoms produced through volume reactions in the IR and coming from the target are lost as they diffuse out of the IR, described by the loss term

$$R_{\rm n,diff} = \frac{\Gamma_{\rm n,diff}}{L} \tag{4}$$

where $\Gamma_{\rm n,diff}$ is the flux of neutral atoms or molecules, and $L = z_2 - z_1$ is the distance through the IR, which represents the typical length that species with a directed flow from the target travel when diffusing out of the IR. The flux is

$$\Gamma_{\rm n,diff} = \Gamma_{\rm n,0} \exp\left(\frac{-L}{\lambda_{\rm n,Ar}}\right) \tag{5}$$

where $\lambda_{\rm n,Ar}$ is the mean free path for a target atom and $\Gamma_{\rm n,0}$ is the random flux governed by the thermal velocity of the particle coming off the target. We herein approximate the sputtered Ti neutral-neutral cross section with a typical effective momentum-exchange cross section of 2×10^{-19} m^{-2} [27]. Approximating with billiard-ball collisions, this value is taken to be independent of the energies of the neutral populations. The velocity of the particle coming off the target is

$$v_{\rm ran} = \langle |v_z| \rangle = \sqrt{\frac{2eT_{\rm n}}{\pi m_{\rm n}}} \tag{6}$$

and $T_{\rm n}$ is the temperature for the neutral species n. The cathode target of a magnetron is heated by ion bombardment which leads to an elevated gas temperature close to the target. In addition there can during the pulses be a time variation of the gas temperature due to the sputter wind. Both processes have been measured by tunable diode laser absorption spectroscopy (TD-LAS) in a discharge for which an elevated gas temperature was included in the IRM [9]. In the present work, however, we lack a measured value and therefore the gas temperature in the model is kept constant at 300 K.

For the terms $R_{\rm g,refill}$, $R_{\rm g,kick-out}$, and $R_{\rm g,return}$, we will focus on the neutral species of

the working gas, here argon. It is well known that gas rarefaction lowers the density of the working gas inside the IR below the value in the surrounding gas reservoir, $n_{\rm g,0}$ [28–31]. This gives a back-diffusion (gain) term

$$R_{\rm g,refill} = \frac{1}{2} v_{\rm g,ran} \frac{(n_{\rm g,0} - n_{\rm g}) S_{\rm RT}}{V_{\rm IR}} \tag{7}$$

where the subscript g stands for the atoms of the working gas and $v_{\rm ran}$ is their random thermal velocity as defined in Eq. (6). In the present case, the argon gas diffusional refill term is determined by the gas temperature and the gas density difference $(n_{\rm Ar,0} - n_{\rm Ar})$ between the IR and the surrounding volume. By definition, only atoms moving towards the boundary are involved so that the densities are taken to be one half of the volume densities.

In the IRM, gas rarefaction by the effect of the sputter wind [28] is implemented as an argon kick-out term by collisions with fast sputtered particles coming from the target. For each of the neutrals Y of the working gas, including the metastable states, the particle balance includes a loss term

$$R_{\rm n,kick-out} = \frac{1}{2} \frac{v_{{\rm ran},X}}{L} F_{\rm coll} \frac{m_X}{m_Y} \frac{\sum n_{X,i}}{\sum_i n_{Y,i}} n_Y \tag{8}$$

where X here stands for the species sputtered off the target and their ions, singly and doubly ionized. The sum is taken over all the states of that sputtered species. A multiplication of the flux reductions by the mass ratio $m_{\rm M}/m_{\rm Ar}$ accounts for the conservation of momentum. $F_{\rm coll} = 1 - \exp(-L/\lambda_{\rm M,Ar})$ is the probability of a collision inside the IR [4], and $\lambda_{\rm M,Ar}$ is defined as above. As an example, the kick-out term for the ground state neutral argon density equation is, in the IRM, given as

$$R_{\rm Ar,kick-out} = [(\Gamma_{\rm M,0} - \Gamma_{\rm M,diff}) + (\Gamma_{\rm M^+,0} - \Gamma_{\rm M^+,diff}) + (\Gamma_{\rm M^{2+},0} - \Gamma_{\rm M^{2+},diff})] \frac{S_{\rm BP}}{V_{\rm IR}} \frac{m_{\rm M}}{m_{\rm Ar}} \frac{n_{\rm Ar}}{n_{\rm Ar} + n_{\rm Ar^m}}. \tag{9}$$

where we have replaced $(1/2) v_{{\rm ran},X} \sum n_{X,i}$ in Eq. (8) with the flux $\sum \Gamma_{X,i}$, and $S_{\rm BP}$ is the area of the annular cylinder facing the lower density plasma outside the IR (bulk plasma). The outwards argon momentum gain is thereby obtained through the reduction of metal outwards momentum flow, and is therefore proportional to the flux difference between the

metal (atoms and ions) outwards fluxes that would be obtained in the absence of collisions with argon (indexed 0 in the equation) and the actual metal fluxes that are reduced by momentum exchange collisions (indexed diff).

In the IRM, we do not only consider cold argon neutrals with density $n_{\mathrm{Ar^C}}$ and metastable argon with density $n_{\mathrm{Ar^m}}$, but also two populations originating from argon ions that bombard the target and then return to the discharge volume as neutrals: warm argon atoms with density $n_{\mathrm{Ar^W}}$ and hot argon atoms with density $n_{\mathrm{Ar^H}}$. The hot component is assumed to return almost immediately, after mixing in the hot spot created by the ion impact. It is therefore ascribed a temperature with an energy of the same order as the sputtered species, typically a few eV. The warm population $\mathrm{Ar^W}$ is assumed to first penetrate the target surface, and then slowly diffuse back as atoms. Its energy is taken to be the thermal energy of the surface, with about 0.1 eV ($\sim$ 1000 K) as an upper bound [25]. Furthermore, a fraction $\xi_{\mathrm{pulse}}\xi_{\mathrm{H}}$ of the recombined $\mathrm{Ar^+}$ ions is assumed to return as hot neutrals $\mathrm{Ar^H}$ during the pulse, and a fraction $\xi_{\mathrm{pulse}}(1-\xi_{\mathrm{H}})$ is assumed to return as warm neutrals $\mathrm{Ar^W}$ during the pulse. The hot argon atoms are approximated to have an effective temperature of 4/3 eV (average energy of 2 eV) based on computer simulations [5]. Here ξ_{pulse} is a parameter that tells how much of the trapped Ar is returning during the pulse. In the present case we assume $\xi_{\mathrm{pulse}} = 1$ (i.e. 100 % of the Ar returns during the pulse). The choice of $\xi_{\mathrm{pulse}} = 1$ is motivated elsewhere [5, 7]. As default we therefore use a standard set: 50 % are $\mathrm{Ar^W}$ with $T_{\mathrm{Ar^W}} = 0.1$ eV, and 50 % are $\mathrm{Ar^H}$ with $T_{\mathrm{Ar^H}} = 2$ eV. Thus, for hot argon neutrals $\mathrm{Ar^H}$ there is a generation term

$$R_{\mathrm{Ar^H,return}} = \xi_{\mathrm{pulse}}\xi_{\mathrm{H}}\Gamma^{\mathrm{RT}}_{\mathrm{Ar^+}}\frac{S_{\mathrm{RT}}}{V_{\mathrm{IR}}} \tag{10}$$

where V_{IR} is the volume of the IR, and $\Gamma^{\mathrm{RT}}_{\mathrm{Ar^+}}$ is the flux of $\mathrm{Ar^+}$ ions towards the target. For the generation of warm neutrals ξ_{H} is replaced by $(1-\xi_{\mathrm{H}})$ in the term above. Coming from the target, the hot argon neutrals $\mathrm{Ar^H}$ and the warm argon neutrals $\mathrm{Ar^W}$ have a directed flux away from the target, giving a loss out of the IR at random velocity (Eq. (6) above), and thus a loss rate

$$R_{\mathrm{Ar^Z,loss}} = v_{\mathrm{ran}} n_{\mathrm{Ar^Z}}\frac{S_{\mathrm{RT}}}{V_{\mathrm{IR}}} \tag{11}$$

where Z stands for H for hot and W for warm argon atoms.

The need to assume the two parameters ξ_{pulse} and ξ_{H} for the recombined Ar atoms from the target is one of the weak points of the IRM model. If accurate modeling of gas recycling

is desired, these should either be varied to test their influence as in Huo et al [5, 7, 8], or the values be assessed separately. For the present discharge the sensitivity analysis showed a small importance of gas recycling. We therefore simply put $\xi_{\rm H}$ in the middle of the possible range 0 to 1. We want to stress, however, that it sometimes might be important to choose the parameters for the $\rm Ar^H$ and $\rm Ar^W$ populations with more care. This would typically be the case if the magnetron has a larger size, or if the plasma density and/or electron temperature are higher. These changes should increase the probability of ionization of the hot and the warm argon gas components, followed by back-attraction to the target. The existence of discharges where this process is even dominating the discharge has been demonstrated by Anders et al. [25]. Using a discharge with a graphite target, they demonstrated that an argon gas recycling trap can develop if the current is high enough. Furthermore, we have demonstrated that working gas recycling dominates a reactive HiPIMS discharge operated in the poisoned mode [11].

2. *Ion particle balance*

For each ion there is a loss rate given as

$$R_{i,\rm loss} = \frac{\Gamma_i^{\rm BP} S_{\rm BP} + \Gamma_i^{\rm RT} S_{\rm RT}}{V_{\rm IR}} \tag{12}$$

where i stands for the particular ion, and $\Gamma_i^{\rm BP}$ is the flux of ion i across the boundary towards the lower density plasma. However, even though most of the potential falls across the sheath, a fraction of the potential generally penetrates into the ionization region [32]. Thus the ions have a larger probability to be attracted back to the target. To account for this, we have added an adjustable probability β that accounts for the back-attraction of ions. Thus the flux density out of the IR towards the lower density plasma is reduced as required to obtain the assumed ion back-attraction probability β

$$\Gamma_i^{\rm BP} = \left(\frac{1}{\beta} - 1\right) \frac{S_{\rm RT}}{S_{\rm BP}} \Gamma_i^{\rm RT} \tag{13}$$

In earlier versions of the model [4, 26] it was assumed that the ions cross the sheath edge at the racetrack with the Bohm speed. This assumption turns out to be inconsistent with a significant potential drop over the extended presheath, in the range 10 – 100 V, as have

been observed recently in the HiPIMS discharge [17, 33]. An improved treatment is therefore presented here and used for the calculations. Instead of accounting for spread-out ionization within the IR at various distances from the target we make an approximation based on average quantities. The main assumptions are that the average ion that ends up at the target was produced in the middle of the IR, at a distance $(z_2 - z_1)/2$ from the sheath edge, and that the potential difference from this position to the sheath edge is $U_{\rm IR}/2$. The loss time in the IR for this average ion is under these assumptions

$$t_{\rm loss} = \frac{z_2 - z_1}{\sqrt{\frac{q_i U_{\rm IR}}{m_i}}}. \tag{14}$$

The number of ions in the IR is

$$n_i V_{\rm IR} = n_i S_{\rm RT}(z_2 - z_1). \tag{15}$$

Since only a fraction β of the ions are destined to go to the racetrack the total flux towards the race track can be written as $\beta\times$ (number of ions in IR)/(loss time). Notice that this implies that $t_{\rm loss}$ of Eq. (14) is valid also for ions that go to the bulk plasma. We use this as a first approximation for high β values. This gives

$$\Gamma_i^{\rm RT} S_{\rm RT} = \frac{\beta n_i S_{\rm RT}(z_2 - z_1)}{t_{\rm loss}}. \tag{16}$$

Division by $S_{\rm RT}$ gives the flux to the racetrack

$$\Gamma_i^{\rm RT} = \beta n_i \sqrt{\frac{q_i U_{\rm IR}}{m_i}} \tag{17}$$

where q_i is the ion charge and $U_{\rm IR}$ the potential drop over the IR.

3. *Electron balance*

In the IRM, two electron populations are implemented: one cold, $e^{\rm C}$, and one hot, $e^{\rm H}$. They are related to the cold electrons found in the IR and the hot secondary electrons ejected from the cathode, and are described in more detail in section II B where the power balance is discussed. Concerning the particle balance, the discharge is assumed to be quasi-neutral

and the density of the cold electrons is given by

$$n_{\rm ec} = \sum_i Z_i n_{+,i} - \sum_j n_{-,j} - n_{\rm eh} \tag{18}$$

where Z_i is the charge state of the positive ion, $n_{+,i}$ is the density of the positive ion i, $n_{-,i}$ is the density of the negative ion i, and where the density of the hot electrons is obtained from their effective electron temperature $T_{\rm eH}$ and their electron energy density $p_{\rm eH}$ (see section II B) as

$$n_{\rm eh} = \frac{p_{\rm eH}}{eT_{\rm eH}} \tag{19}$$

The assumption of quasi-neutrality in the IRM is used only to obtain the electron density in the ionization region from the total ion charge density through Eqs. (18) and (19). When used for this limited purpose it is valid under the condition $\lambda_{\rm D}/l_{\rm c} \ll 1$, where $\lambda_{\rm D}$ is the Debye length and $l_{\rm c}$ is the system length scale, which, for HiPIMS discharges, is satisfied by typically more than three orders of magnitude. Please notice that the quasi-neutrality assumption gives neither values nor constraints regarding the electric fields and potentials. These are in the IRM instead assessed through the power balance as described in section II B.

B. Power balance

The power balance equates the power absorbed by the plasma electrons to power losses due to processes, such as elastic and inelastic collisions, de-excitation processes, and Penning ionization. Before treating the power balance, we will first describe the cold and hot electron populations and how electrons are heated. The use of two electron populations have essentially two effects. First, this treatment gives a more accurate account of the cost of ionization as a function of electron energy. For example, metal ionization degree, degree of self-sputtering, and bulk electron temperature tend to decrease, while gas rarefaction and plasma density tend to increase, as compared to the first version of the IRM where only one electron population is assumed [4]. These trends can be understood from the lower energy cost of ionization by the now introduced population of hot electrons. Second, this makes it possible to quantify two mechanisms of electron heating: secondary electron acceleration across the sheath and Ohmic heating in the IR. The power transfer to the electrons is given

by

$$P_{\rm e} = P_{\rm SH} + P_{\rm Ohm} \tag{20}$$

where $P_{\rm e}$ is split up into sheath energization $P_{\rm SH}$ and Ohmic heating $P_{\rm Ohm}$ in the ionization region. This is achieved by splitting the discharge voltage up into the potential drop over the sheath and the potential drop over the ionization region, $U_{\rm D} = U_{\rm SH} + U_{\rm IR}$, as shown in Figure 1. In each volume, the electrons get a part of the total electric power, $I_{\rm D}U_{\rm SH}$ and $I_{\rm D}U_{\rm IR}$ respectively, that is given by the fraction of the current the electrons carry.

The electron current in the sheath is obtained from the model-calculated ion currents to the target as

$$P_{\rm SH} = I_{\rm e,SH}U_{\rm SH} = \left(I_{\rm Ar^+}\gamma_{\rm Ar^+,eff} + \frac{1}{2} I_{\rm M^{2+}}\gamma_{\rm M^{2+},eff} \right) U_{\rm SH}. \tag{21}$$

where $\gamma_{\rm Ar^+,eff} = \gamma_{\rm Ar^+} m\epsilon_{\rm e}(1-r)$ is the effective secondary electron emission yield for $\rm Ar^+$-ions bombarding the target and $\gamma_{\rm M^{2+},eff} = \gamma_{\rm M^{2+}} m\epsilon_{\rm e}(1-r)$ is the effective secondary electron emission yield for doubly ionized metal ions bombarding the target, and $\epsilon_{\rm e}$ represents the fraction of the electron energy that is used for ionization before being lost from the discharge process [22]. The terms within the parenthesis to the right gives the number of secondary electrons that are emitted by argon ions $I_{\rm Ar^+}\gamma_{\rm Ar^+}$ and twice ionized metal ions $I_{\rm M^{2+}}\gamma_{\rm M^{2+}}$ from the target. The number of electrons that actually leave the cathode is reduced by the recapture probability r, while a factor m (equal or greater than unity) accounts for ionization within the sheath [34]. The factor 1/2 in front of the second term accounts for the fact that each $\rm M^{2+}$ ion carries a charge 2e. There is no $I_{\rm M^+}\gamma_{\rm M^+}$ term because secondary emission coefficient of the single ionized metal $\gamma_{\rm M^+} = 0$ for the ion energy range studied here, below 1 keV [35].

In the ionization region the electrons are heated by Ohmic heating [7] given by

$$P_{\rm Ohm} = I_{\rm e,IR}U_{\rm IR} = \left\langle \frac{J_{\rm e}}{J_{\rm D}} \right\rangle I_{\rm D}U_{\rm IR} \tag{22}$$

Here $\langle J_{\rm e}/J_{\rm D}\rangle$ is the volume average of the fraction of the discharge current in the IR that is carried by electrons, as shown in the right half of Figure 1. As an average over the ionization region we typically take $\langle J_{\rm e}/J_{\rm D}\rangle \sim 1/2$ [7]. The sheath potential is given by $U_{\rm SH} = U_{\rm D} - U_{\rm IR}$. In the IRM, $U_{\rm IR}$ is defined as a fraction of the total input discharge voltage, $U_{\rm IR} = fU_{\rm D}$ (see also Section V).

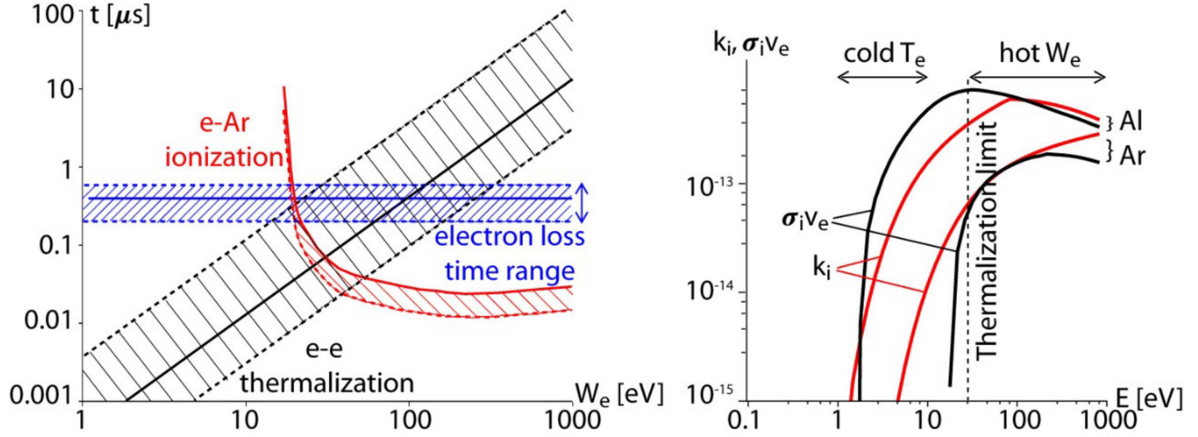

FIG. 2: Data used to motivate the simplified treatment of the EEDF, as a hot tail with a close to constant ionization rate coefficient and a cold population with a thermal distribution. (a) Time constants, as function of electron energy, for electron-electron energy exchange, electron loss in collisions with argon, and electron loss out of the ionization region. (b) Rate coefficients for aluminum and argon ionization by electron impact, both from thermal electrons and from mono-energetic distributions.

The two routes of heating are depositing energy into different parts of the electron energy distribution function (EEDF). These electron populations have different ionization rate constants and different effective costs of ionization, and therefore are treated separately as one hot and one cold component. As shown and discussed in detail by Huo et al. [7], a combination of two fortunate circumstance makes it possible to put forward a quite accurate and yet simple model for the ionization rate for the complicated EEDF in HiPIMS discharges. Figure 2 (a) shows, as function of the electron energy, the time constants for three important electron processes: energy loss through ionization of Ar, energy thermalization through Coulomb e-e collisions with the cold background electrons, and the loss of electrons out of the ionization region. The solid lines show these three time constants for typical HiPIMS plasma and gas densities, $n_{\mathrm{e}} = 2 \times 10^{19}$ m^{-3} and gas density $n_{\mathrm{Ar}} = 4.5 \times 10^{20}$ m^{-3} (13.5 mTorr), and dashed areas cover typical variations of these densities between different HiPIMS discharges. The likely fate of an electron that starts at a given energy is determined by the most likely process, i.e., the shortest time constant. We see that there is a division at $\sim$30 eV electron energy: energies below that limit will most quickly become part of a thermal Maxwellian population, while electrons above that energy will be more likely to lose energy in an ionization event. As a result the EEDF below a thermalization limit will be

maintained as a Maxwellian distribution, while in the high energy range it will be spread out in the form of a high energy tail. The first of the fortunate circumstances referred to above is that the whole cold population is kept Maxwellian. This is basically a result of the high plasma density in HiPIMS discharges, and means that for the cold population we need only to keep track of the electron temperature in order to accurately obtain all excitation and ionization rates. The second fortunate circumstance is illustrated in Figure 2 (b) and concerns the high energy tail, above the thermalization limit which here is drawn at 30 eV. The ionization rate coefficient $\sigma_{\rm i} v_{\rm e}$ for Ar by monoenergetic electrons (the black curve) varies quite slowly, only a factor 1.5 in the whole energy range from 30 eV to 1000 eV. The average rate coefficient $\langle \sigma_{\rm i} v_{\rm e} \rangle$ calculated for a Maxwellian distribution varies even less (the red curve), and lies close to the curve for $\sigma_{\rm i} v_{\rm e}$. This means that, to obtain the Ar ionization rate, the most important reaction for the hot tail, do not need to resolve the details of the high energy EEDF – any distribution that has the right number of electrons, and with a reasonable average energy, will give a quite good ionization rate. For simplicity the hot electron population is in the IRM approximated by a Maxwellian. This is made by ascribing a temperature to the hot electrons such that $(3/2)T_{\rm e,hot} = F_{\rm We^H} e U_{\rm D}$, with $F_{\rm We^H} = 0.5$ as a default value. Note that this does not mean we assume the hot population to really have a thermal distribution. Rather, we use the fact that the ionization rate coefficient is insensitive to the actual shape of the hot EEDF and therefore can be approximated by the easily available expression for a thermal distribution.

At each electron impact ionization of the hot electron population the effective cost of ionization $\mathcal{E}_{\rm i,eff}$, and the remaining energy is shared between the two resulting electrons in some statistical manner. If one of the two electrons falls below the e-e thermalization limit ($\approx$ 30 eV in the example chosen above), the hot electron population loses also the energy of this cooler electron. The power balance equation for the hot population for each ionization event includes an average loss due to this process. An ionization then gives an energy loss $\mathcal{E}_{\rm c,eff} + \mathcal{E}_{\rm htc}$ where htc denotes hot-to-cold and $\mathcal{E}_{\rm c,eff}$ is the effective cost of ionization [36, p. 81–82]. The term $\mathcal{E}_{\rm htc}$ also provides an energy input into the cold electron energy equation.

The case where both electrons remain in the hot population also needs a comment. Visualize a hot electrons history as sliding down in energy from the injected beam energy down to the cold population. The distance it travels in energy is proportional to the number

of ionizations made. If both electrons after an ionization fall in the hot population, then the initial hot electron jumps over a distance along the energy axis, and the other electron jumps in at a position to compensate for this reduction in energy. The energy reservoir in the hot population, and hence total number of subsequent ionizations that will be produced, remain the same, while the rate of ionization is doubled as long as both electrons are active. Here we formulate the equations such as they would look if the second electron had dropped immediately into the cold population, keeping in mind that this will give the correct total ionization, but underestimate the instantaneous ionization rate somewhat.

The temporal development of the cold electron temperature is followed by the rate equation

$$
\begin{aligned}
\frac{3}{2}n_{\mathrm{e^C}}\frac{\mathrm{d}T_{\mathrm{e^C}}}{\mathrm{d}t} =& \mathcal{E}_{\mathrm{htc}}\nu_{\mathrm{iz}}^{\mathrm{H}} + \left\langle \frac{I_{\mathrm{e}}}{I_{\mathrm{D}}}\right\rangle_{\mathrm{IR}} f\frac{I_{\mathrm{D}}U_{\mathrm{D}}}{eV_{\mathrm{IR}}} - \frac{T_{\mathrm{e^C}}}{2}\frac{\left(\Gamma_{\mathrm{Ar^+}}^{\mathrm{BP}} + \Gamma_{\mathrm{M^+}}^{\mathrm{BP}} + \Gamma_{\mathrm{M^+}}^{\mathrm{BP}}\right)S_{\mathrm{BP}} + \left(\Gamma_{\mathrm{Ar^+}}^{\mathrm{RT}} + \Gamma_{\mathrm{M^+}}^{\mathrm{RT}} + \Gamma_{\mathrm{M^+}}^{\mathrm{RT}}\right)S_{\mathrm{RT}}}{V_{\mathrm{IR}}} \\
&+ \mathcal{E}_{\mathrm{dex}}k_{\mathrm{dex}}^{\mathrm{C}}n_{\mathrm{Ar^m}} - \left(\mathcal{E}_{\mathrm{dex}} - \mathcal{E}_{\mathrm{iz,M}} - \frac{3}{2}T_{\mathrm{e^C}}\right)k_{\mathrm{P}}n_{\mathrm{Ar^m}}n_{\mathrm{M}} - \left(\mathcal{E}_{\mathrm{c,C,eff}}^{\mathrm{Ar}} + \frac{3}{2}T_{\mathrm{e^C}}\right)k_{\mathrm{iz,Ar}}^{\mathrm{C}}n_{\mathrm{e^C}}n_{\mathrm{Ar}} \\
&- \left(\mathcal{E}_{\mathrm{c,C,eff}}^{\mathrm{Ar^m}} + \frac{3}{2}T_{\mathrm{e^C}}\right)k_{\mathrm{iz,Ar^m}}^{\mathrm{C}}n_{\mathrm{e^C}}n_{\mathrm{Ar^m}} - \left(\mathcal{E}_{\mathrm{c,C,eff}}^{\mathrm{Ar^H}} + \frac{3}{2}T_{\mathrm{e^C}}\right)k_{\mathrm{iz,Ar^H}}^{\mathrm{C}}n_{\mathrm{e^C}}n_{\mathrm{Ar^H}} \\
&- \left(\mathcal{E}_{\mathrm{c,C,eff}}^{\mathrm{Ar^W}} + \frac{3}{2}T_{\mathrm{e^C}}\right)k_{\mathrm{iz,Ar^W}}^{\mathrm{C}}n_{\mathrm{e^C}}n_{\mathrm{Ar^W}} - \left(\mathcal{E}_{\mathrm{c,C,eff}}^{\mathrm{M}} + \frac{3}{2}T_{\mathrm{e^C}}\right)k_{\mathrm{iz,M}}^{\mathrm{C}}n_{\mathrm{e^C}}n_{\mathrm{M}} \\
&- \left(\mathcal{E}_{\mathrm{c,C,eff}}^{\mathrm{M^+}} + \frac{3}{2}T_{\mathrm{e^C}}\right)k_{\mathrm{iz,M^+}}^{\mathrm{C}}n_{\mathrm{e^C}}n_{\mathrm{M^+}} \qquad (23)
\end{aligned}
$$

where f is used as the first fitting parameter, as defined in Table I, and

$$
\nu_{\mathrm{iz}}^{\mathrm{H}} = n_{\mathrm{e^H}}\left(k_{\mathrm{iz,Ar}}^{\mathrm{H}}n_{\mathrm{Ar}} + k_{\mathrm{iz,Ar^m}}^{\mathrm{H}}n_{\mathrm{Ar^m}} + k_{\mathrm{iz,Ar^H}}^{\mathrm{H}}n_{\mathrm{Ar^H}} + k_{\mathrm{iz,Ar^W}}^{\mathrm{W}}n_{\mathrm{Ar^W}} + k_{\mathrm{iz,M}}^{\mathrm{H}}n_{\mathrm{M}} + k_{\mathrm{iz,M^+}}^{\mathrm{H}}n_{\mathrm{M^+}}\right) \qquad (24)
$$

is the ionization frequency [ionizations $\mathrm{m^{-3}s^{-1}}$] of the hot component. In Eq. (23) $\langle I_{\mathrm{e}}/I_{\mathrm{D}}\rangle$ is the average fraction of the current in the ionization region that is carried by electrons, with the default value 0.5 (see discussion by Huo et al. [5]). The first two terms on the right-hand side of Eq. (23) correspond to the energy gain from hot electrons and the total input power, respectively. The third term gives the electron flux across the boundaries of the IR, which is obtained through the sum of the ion fluxes. The remaining terms describe the inelastic collisions. The fourth term is due to electron impact de-excitation of metastable argon atoms

which represents an energy gain term for electrons, the fifth term is to account for Penning ionization of the metal atom, terms six to nine are due to electron impact ionization of argon atoms, the tenth term represents electron impact ionization of the metal atom and the eleventh term represent electron impact ionization of the metal ion which creates M^{2+}. The terms $(3/2)T_e^C$ in Eq. (23) refers to the average energy required for a new free electron to obtain the average cold electron temperature. For details and additions of negative ions, please refer to Gudmundsson et al. [11]. As discussed above, the hot electrons are followed by a rate equation for the density rather than the temperature or average energy:

$$
\begin{aligned}
\frac{\mathrm{d}n_{\mathrm{e^H}}}{\mathrm{d}t} =& \frac{1}{F_{\mathrm{W_e^H}}U_\mathrm{D}} \Bigg[(1-r)\epsilon_\mathrm{e} m \left(\gamma_{\mathrm{Ar^+}} I_{\mathrm{Ar^+}} + \frac{1}{2}\gamma_{\mathrm{M^{2+}}} I_{\mathrm{M^{2+}}}\right) \frac{(1-f)U_\mathrm{D}}{eV_\mathrm{IR}} + \mathcal{E}_\mathrm{dex} k_\mathrm{dex}^\mathrm{H} n_{\mathrm{e^H}} n_{\mathrm{Ar^m}} \\
& - \left(\mathcal{E}_{\mathrm{c,C,eff}}^{\mathrm{Ar}} + \mathcal{E}_\mathrm{htc}\right) k_{\mathrm{iz,Ar}}^\mathrm{H} n_{\mathrm{Ar^m}} n_{\mathrm{e^H}} - \left(\mathcal{E}_{\mathrm{c,C,eff}}^{\mathrm{Ar^m}} + \mathcal{E}_\mathrm{htc}\right) k_{\mathrm{iz,Ar^m}}^\mathrm{H} n_{\mathrm{Ar^m}} n_{\mathrm{e^H}} \\
& - \left(\mathcal{E}_{\mathrm{c,C,eff}}^{\mathrm{Ar^H}} + \mathcal{E}_\mathrm{htc}\right) k_{\mathrm{iz,Ar^H}}^\mathrm{H} n_{\mathrm{Ar^H}} n_{\mathrm{e^H}} - \left(\mathcal{E}_{\mathrm{c,C,eff}}^{\mathrm{Ar^W}} + \mathcal{E}_\mathrm{htc}\right) k_{\mathrm{iz,Ar^W}}^\mathrm{H} n_{\mathrm{Ar^W}} n_{\mathrm{e^H}} \\
& - \left(\mathcal{E}_{\mathrm{c,C,eff}}^{\mathrm{M}} + \mathcal{E}_\mathrm{htc}\right) k_{\mathrm{iz,M}}^\mathrm{H} n_\mathrm{M} n_{\mathrm{e^H}} - \left(\mathcal{E}_{\mathrm{c,C,eff}}^{\mathrm{M^+}} + \mathcal{E}_\mathrm{htc}\right) k_{\mathrm{iz,M^+}}^\mathrm{H} n_{\mathrm{M^+}} n_{\mathrm{e^H}} \Bigg]
\end{aligned} \quad (25)
$$

The square bracket keeps track of the rate of change of the total energy in the hot population. The first term inside the bracket is the energy obtained by the hot electrons through the sheath. The other terms describe the inelastic collisions of the hot electrons. Losses across the boundaries are neglected as discussed above. Dividing the total energy by the average energy of the hot electrons ($F_{\mathrm{W_e^H}}U_\mathrm{D}$) gives the density.

III. PLASMA CHEMISTRY

The Ar^+-ions are treated as one population in all versions of IRM. The rate equation for $n_{\mathrm{Ar^+}}$ therefore contains gain terms representing ionization from the hot and warm populations of argon atoms. The energy loss per electron-ion pair created by the cold electron population for the argon atom in the ground state is calculated as discussed by Hjartarson et al. [37] assuming a Maxwellian EEDF. The argon reaction set and rate coefficients used in the model are listed in table III. The rate coefficients are calculated assuming a Maxwellian EEDF and for the cold electrons valid in the range 1 – 7 eV and for the hot electrons valid in the range 200 – 1000 eV. The argon reaction set is rather simple as we consider only argon

atoms in the ground state and metastable argon atoms where the two 4s metastable levels ($^3P_0$ and $^3P_2$) are combined to give one effective metastable species.

Here we study two discharges where metal atoms and ions are aluminum or titanium. We assume that metal ions are created by electron impact ionization, by Penning ionization, collisions of metal atoms with electronically excited argon atoms (Ar^m + M $\longrightarrow$ M^+ + Ar + e) with a rate coefficient k_P = 5.9 $\times$ 10^{16} m^3 s^{-1} for Al [38] and 3.17 $\times$ 10^{-15} m^3 s^{-1} for Ti [9], and through charge exchange Ar^+ + M $\longrightarrow$ M^+ + Ar with a rate coefficient $k_{chexc} = 1 \times 10^{-15}$ m^3 s^{-1} [38].

The rate coefficient for the electron impact ionization of aluminum is calculated from the electron impact ionization cross sections given by Freund et al. [39]. The rate coefficient for electron impact ionization of Al^+ to create Al^{2+} is based on the cross sections given by Hayton and Pert [40] and McGuire [41]. The first ionization potential of Al is 5.99 eV while the second ionization potential is 18.8 eV. The collision energy loss $\mathcal{E}_c^{Al}$ per electron-ion pair created for the aluminum atom is calculated using the electron impact ionization cross section, electron impact excitation cross section (to levels 4s, 3d and 4p only) and elastic cross sections calculated by Wells and Miller [42].

The electron impact ionization cross section for Ti is taken from Bartlett et al. [43] and Deutsch et al. [44] and the electron impact ionization cross section for Ti^+ to create Ti^{2+} is taken from the measurements of Diserens et al. [45]. The first ionization potential of Ti is 6.82 eV while the second ionization potential is 13.58 eV. The rate coefficients for ionization of Ti and Ti^+ are listed in table III. To calculate $\mathcal{E}_c^{Ti}$ for Ti, we use the electron impact ionization cross section [43, 44] with ionization potential of 6.828 eV. Furthermore we include the 9 lowest excited levels located at 0.81, 0.9, 1.43, 1.97, 2.09, 2.29, 2.40, 2.47 and 2.66 eV and assume that each excitation cross section follows the Thomson cross section [36, p. 72] with a peak at 1/5 of the peak of the ionization cross section. The cross section for electron elastic scattering by Ti is assumed to be the same as for nitrogen atoms [46, 47].

For the secondary electron emission yield for argon ions bombarding an aluminum target we use the values measured by Yamauchi and Shimizu [48]. A fit to their measured values in the range 700 – 1500 V gives $\gamma_{Ar^+} = 0.0769 + E_{Ar^+} \times 1.1823 \times 10^{-5}$, where E_{Ar^+} is the Ar^+-ion bombarding energy in eV, which we extend to zero energy. For self-sputtering Al^+ $\longrightarrow$ Al we use $Y_{self} = 0.016 E_{Al^+}^{2/3}$, based on the data collected by Hayward and Wolter [49] and the calculation by the SRIM code given by Anders et al. [16]. For argon sputtering

aluminum $Ar^+ \longrightarrow Al$ we use the sputtering data collected by Ruzic [50] which up to 1000 eV is well fitted as $Y_{\rm sput} = 2.16 \times 10^{-3} E_{\rm Ar^+}$. For self-sputtering $Ti^+ \longrightarrow Ti$ and $Ti^{2+} \longrightarrow Ti$ and for argon sputtering titanium $Ar^+ \longrightarrow Ti$ we use a fit to the data given by Anders et al. [16].

TABLE III: The reaction set for electron–argon and argon–argon reactions. The rate coefficients are calculated assuming a Maxwellian electron energy distribution function and fit in the range $T_e = 1 - 7$ V for cold electrons and $200 - 1000$ V for hot electrons.

	Reaction	Rate coefficient (cold) [m^3/s]	Rate coefficient (hot) [m^3/s]	Ref
(R1)	$e + Ar \rightarrow Ar^+ + e + e$	$2.34 \times 10^{-14}\ T_e^{0.59}\ e^{-17.44/T_e}$	$8 \times 10^{-14}\ T_e^{0.16}\ e^{-27.53/T_e}$	[51]
(R2)	$e + Ar^m \rightarrow Ar^+ + e + e$	$6.8 \times 10^{-15}\ T_e^{0.67}\ e^{-4.2/T_e}$	$5.7 \times 10^{-13}\ T_e^{-0.33}\ e^{-6.82/T_e}$	[52]
(R3)	$e + Ar \rightarrow Ar^m + e$	$2.5 \times 10^{-15}\ T_e^{0.74}\ e^{-11.56/T_e}$	$3.85 \times 10^{-14}\ T_e^{-0.68}\ e^{-22/T_e}$	[52]
(R4)	$e + Ar^m \rightarrow Ar + e$	$4.3 \times 10^{-16}\ T_e^{0.74}$	$4.3 \times 10^{-16}\ T_e^{0.74} + 4.957 \times 10^{-14}\ T_e^{-0.39}\ e^{-7.78/T_e} + 2.67 \times 10^{-15}$	[53]
(R5)	$e + Ti \rightarrow Ti^+ + e$	$2.8278 \times 10^{-13} T_e^{-0.0579}\ e^{-8.7163/T_e}$	$1.1757 \times 10^{-12} T_e^{-0.3039}\ e^{-21.1107/T_e}$	[43,
(R6)	$e + Ti^+ \rightarrow Ti^{2+} + e$	$1.8556 \times 10^{-14} T_e^{0.4598}\ e^{-12.9927/T_e}$	$8.1858 \times 10^{-12} T_e^{-0.669}\ e^{-200.93/T_e}$	[45]
(R7)	$Ar^+ + Ti \rightarrow Ar + Ti^+$	1×10^{-15}		[a]
(R8)	$Ar^m + Ti \rightarrow Ar + Ti^+ + e$	3.17×10^{-15}		[9]
(R9)	$e + Al \rightarrow Al^+ + e$	$1.3467 \times 10^{-13} T_e^{0.3576} \exp(6.7829/T_e)$	$\exp\left(-0.074347[\log(T_e)]^2 + 0.637867 \log(T_e) - 29.516747\right)$ if $T_e > 81$ eV	[39]
(R10)	$e + Al^+ \rightarrow Al^{2+} + e$	$2.34 \times 10^{-14} T_e^{0.59} \exp(-17.44/T_e)$	$\exp\left(-0.1008[\log(T_e)]^2 + 1.2011 \log(T_e) - 34.5841\right)$ if $T_e > 7$ eV	[40,
(R11)	$e + Al \rightarrow Al(4s) + e$	$1.821 \times 10^{-12} T_e^{0.8679} \exp(6.975/T_e)$		[42]
(R12)	$e + Al \rightarrow Al(3d) + e$	$5.7148 \times 10^{-12} T_e^{-1.2858} \exp(6.975/T_e)$		[42]
(R13)	$e + Al \rightarrow Al(4p) + e$	$1.7195 \times 10^{-12} T_e^{-1.3692} \exp(9.0616/T_e)$		[42]
(R14)	$e + Al^+ \rightarrow Al + e$	$10^{[0.0104(\log(E))^2 + 0.1134(\log(E)) - 11.700]}$		[42]
(R15)	$Ar^+ + Al \rightarrow Ar + Al^+$	1×10^{-15}		[38]
(R16)	$Ar^m + Al \rightarrow Ar + Al^+ + e$	5.9×10^{-16}		[38]

[a] Estimated due to lack of data

IV. EXPERMENTAL DETAILS

The model is applied to explore two sets of experimental data. The first set is from an argon discharge with an Al target performed at the Lawrence Berkeley National Laboratory [16] and the second set is from an argon discharge with a Ti target performed at the University of Liverpool [54–56].

A. Argon discharge with Al target

The first set of experiments, here used as input to the IRM, were performed by Anders et al. [16] using a planar, balanced magnetron equipped with an Al target. The target was 50 mm in diameter and 6.25 mm thick and the diameter of the circular race track was 25 mm. The power was supplied by a SPIK2000A pulse power supply operated under a pressure of 1.8 Pa in an Ar atmosphere. The gas was supplied near the target and the total pressure was monitored by an MKS Baratron gauge. Unipolar pulses with a fixed discharge

voltage were applied to the cathode. The nominal voltage was adjustable up to 1000 V, the arc threshold was set to 120 A, and the pulse length was 400 μs. This power supply maintains the discharge voltage throughout the full pulse length. Further details concerning the experimental conditions can be found elsewhere [16].

The measured temporal variation of the discharge current for various constant square discharge voltages is shown in Figure 3 (a). One common feature of these current-time traces is that they all have a peak followed by a steady plateau stage. The initial current peak current value depends on the applied voltage, the peak value increases with increased discharge voltage. According to Anders et al. [16], the current goes through the initial pressure-dependent and working gas dominated phase to a later power-dependent and target material-dominated phase that involves self-sputtering. In the present work, the whole set of experimental discharge conditions seen in Figure 3 (a) were investigated using the IRM model to see if the model was able to reproduce the currents during all the peak and plateau phases.

B. Argon discharge with Ti target

The second set of experiments were performed by Mishra et al. [54–56] using a 150 mm diameter Ti target. During the experiment the magnetic field strength was changed by moving the inner or outer magnetic poles. The HiPIMS discharges were generated by a SINEX 3.0 HiPIMS power supply operated in an argon atmosphere at a pressure of 0.54 Pa. The experiments were conducted at three different pulse frequencies (75 Hz, 100 Hz, and 150 Hz) and four different magnetic field strengths here denoted BF1 to BF4 [54, 55]. The HiPIMS discharge pulse width was in all cases set to 100 μs. BF1 represents the strongest magnetic field configuration with a total magnetic field strength $|\mathbf{B}|$ at the target surface of the race track of about 380 Gauss. By pulling back the magnets behind the target, the magnetic field strength $|\mathbf{B}|$ was progressively lowered to 320, 250, and 180 Gauss at the same position, corresponding to BF2, BF3, and BF4 cases, respectively. The field strengths were determined from bench measurements of the magnetic field taken in the axial (B_z) and radial directions (B_r) using a Hall probe [56]. Examples of the spatially resolved magnetic field maps are given by Mishra et al. [54]. The temporal variation of the discharge current and voltage for the Ti target for various magnetic field strengths for the three pulse frequencies

is shown in Figure 4. This power supply does not maintain the voltage throughout the full pulse length and the voltage decreases with time during the pulse.

V. MATCHING THE MODEL TO EXPERIMENTAL DATA

The discharge voltage $U_{\mathrm{D}}(t)$ is used as an input variable and therefore an energetically self-consistent model run is obtained when modeled and experimentally determined discharge currents agree, i.e. $I_{\mathrm{Calc}} = I_{\mathrm{D}}(t)$. The model current is calculated at the target surface as

$$I_{\mathrm{Calc}} = eS_{\mathrm{RT}}\Gamma_{\mathrm{Ar^+}}(1+\gamma_{\mathrm{Ar^+,eff}}) + eS_{\mathrm{RT}}\Gamma_{\mathrm{M^+}}(1+\gamma_{\mathrm{M^+,eff}}) + eS_{\mathrm{RT}}\Gamma_{\mathrm{M^{2+}}}(2+\gamma_{\mathrm{M^{2+},eff}}) \qquad (26)$$

Here, Γ_i represent the different ion fluxes (particles per m^2 and s), as they enter the cathode sheath, S_{RT} is the area of the race track, and $\gamma_{i,\mathrm{eff}}$ represent the various effective secondary electron emission yields due to ions (i) bombarding the target.

Three model fitting parameters are used. The first fitting parameter is the probability for ions present in the IR to leave this volume toward the target, denoted β. In the literature, this parameter is often referred to as the ion back-attraction probability for the metal ion [57]. Typically we use the same value of β for the ions of the working gas and for the metal ions in our IRM runs. The second fitting parameter is the potential drop across the IR, U_{IR}, which was discussed in the introduction and seen in Figure 1. In practice, U_{IR} is set using the ratio of U_{IR} to the discharge voltage U_{D} denoted by f, i.e. $f = U_{\mathrm{IR}}(t)/U_{\mathrm{D}}(t)$, see also table I. The described treatment gives a two-dimensional parameter space for model fitting. In the fitting procedure, the value of β is varied in the range from 0 to 1 and, for each β, the value of U_{IR} is selected that gives the best fit of $I_{\mathrm{Calc}}(t)$ to the experimentally determined discharge current waveform $I_{\mathrm{D}}(t)$. For the discharges with an Al target, the third fitting parameter, the electron recapture probability r, can be varied in the full range $0 \leq r \leq 1$ without influencing the model output significantly. Here only the two first fitting parameters are needed. The best reproduced currents by the model are shown in Figure 3 (b). By comparing Figures 3 (a) and (b) we see that the calculated current matches the measured current very well over the complete voltage and time range investigated. In all cases reported here, the calculated currents match the experimental discharge currents

TABLE IV: The values of the three parameters β, $f = U_{IR}/U_D$ and r, that lock the model for the cases explored here.

	Al target	Ti target
β	0.9	0.8
r	0.5	0.84
f	0.163 – 0.289	0.117 – 0.182

within ±20 % at all times throughout the pulse. For a discharge with Ti target three fitting parameters are needed, in addition to β and U_{IR} the recapture probability of electrons r influences the current fitting. The values of the three parameters β, $f = U_{IR}/U_D$ and r that lock the model for the cases explored here are summarized in Table IV. The ion back-attraction probability β is slightly lower (0.8) when operating with a Ti target than when operating with an aluminum target (0.9). The fraction of the applied voltage that drops over the ionization region increases with decreasing discharge voltage from 0.163 U_D of 1000 V to 0.289 for 360 V when operating with aluminum target. For the discharge with Ti target the fraction of the applied voltage that drops over the ionization region is highest or 0.182 at 75 Hz and the second strongest magnetic field and lowest for 150 Hz and the weakest magnetic field or 0.117.

The best reproduced currents for the discharges with Ti target operated at different pulse frequencies and magnetic field strength are shown in Figure 4 (c), (f), and (i) for pulse frequency of 75, 100 and 150 Hz, respectively. Note that the magnetic field is not taken into account in the IRM so the variation in the parameters due to the magnetic field is only observed indirectly. When the magnetic field is changed in the experiment there is a change in the discharge current waveform. When the IRM is then adapted to the new waveform, the internal discharge chemistry becomes that of the discharge with the changed magnetic field. By comparing Figures 3 (a) and (b) on one hand and Figures 4 (b) and (c), (e) and (f), and (h) and (i) on the other hand, it is concluded that the IRM could follow the current trends closely and match the discharge currents within the acceptable error range for all discharges investigated, for both short and long pulses and for both a fixed discharge voltage and a discharge voltage that varies within the pulse.

A. Sensitivity analysis

Besides the fitting parameters β, $f = U_{\rm IR}/U_{\rm D}$, and r, there are a few additional internal parameters in the IRM that can be adjusted based on the experimental conditions. We here consider how these influence the results of the model. They include the energy loss to the cold electron population when hot electrons ionize $\mathcal{E}_{\rm htc}$, the recycle parameters $\xi_{\rm pulse}$ and $\xi_{\rm H}$ for the process gas, and the dimension of the ionization region z_2.

We want to find how the model output varies when varying these parameters. This is directly linked to the important question of how simple the model can be made to reach the same level of self-consistency. Which processes can be left out so that by only adjusting the remaining fitting parameters within a reasonable range gives similar goodness of fits ? For one aspect of the model the answer is clear: a model without Ohmic heating can generally not be made self-consistent from an energy point of view. With realistic secondary electron emission coefficients, electrons accelerated across the sheath simply do not carry enough energy to reproduce real experiments with a measured currents at an applied voltage [8]. Regarding other components of the model the answer varies depending on the target material, the current density, and the target size. The simple rule of thumb is that the model is insensitive to processes that are not important in the discharge. For a 50 mm diameter Al target, a sensitivity analysis in [8] showed that the model results were quite insensitive both to the assumed value of the electron recapture probability r and the efficiency factor $F_{\rm recycle}$ for gas recycling. In this discharge, secondary electrons and recycled process gas were both shown to be unimportant. For the discharge studied in the present work with a 150 mm diameter Ti target, a similar sensitivity analysis (not shown) reveals a large sensitivity to r, but still a small sensitivity to $F_{\rm recycle}$. This is consistent the finding that secondary electrons play a significant role, but not gas recycling. Here, r is needed as a third model fitting parameter besides β and $U_{\rm IR}$. Finally, for a fully oxygen-poisoned 75 mm diameter Ti target studied by Gudmundsson et al. [11], both secondary electrons and gas recycling needed to be included. We propose that, in order to determine how simple the model can be made in a special case, one has to run the complete version and identify possible unimportant processes.

In Huo et al. [8] the two parameters $\xi_{\rm pulse}$ and $\xi_{\rm H}$ are combined into one single parameter, $F_{\rm recycle}$ that quantifies the argon gas recycling efficiency. The returning fluxes during the

pulse of hot and warm argon are a fraction ($\xi_{\rm pulse}\xi_{\rm H}$) and ($\xi_{\rm pulse}(1-\xi_{\rm H})$), respectively, of the total influx of argon ions to the target. The most efficient recycling of argon, $F_{\rm recycle}=1$, is obtained when all the argon returns during the pulse and at the target temperature. The opposite, and the most inefficient recycling, corresponds to $F_{\rm recycle}=0$, when all the argon returns between the pulses and thereby is not involved in the discharge. $F_{\rm recycle}=0.5$ is when all the argon, half hot and half warm, returns to the discharge during the pulse. Please note that $F_{\rm recycle}=1$ only means that the parameters $\xi_{\rm pulse}$ and $\xi_{\rm H}$ are set to the values that give maximum recycling which is then calculated by the model. The recycled fraction of Ar can be very small even if $F_{\rm recycle}=1$. One such case is described by Huo et al. [8], and identified as due to a small probability of ionization of argon atoms during their transit from the target through the IR.

In conclusion, we find that the model is robust against changes of additional internal parameters (within reasonable ranges) and that two fitting parameters are sufficient for the Al target while three are needed for the Ti target. Finally, we see in Table IV, that f is always in the range $0.11-0.29$ which means that the voltage drop across the IR is in the range $100-163$ V.

VI. RESULTS AND DISCUSSION

Here we discuss the results of the model runs for the two different experimental setups. In particular we explore the ionization fractions, the electron heating mechanisms and the discharge current composition. Furthermore, we compare the results from a discharge with Al target to a discharge with Ti target. In the present work we have focused on the ions and electrons and will show that the ion composition, in the current at the target surface, holds the key to the differences between the investigated discharges targets materials Al and Ti, while the electron energization determines the effect of varying the magnetic field strength.

A. Differences between the discharges

Let us first look at the data, before giving physical explanations. Figure 5 (a) - (c) shows the temporal behavior of the ionization degree, $n_{\rm i}/(\sum n_{{\rm i},i}+n_{\rm n})$, for (a) $n_{\rm i}=n_{\rm Ar^+}$, (b) $n_{\rm i}=n_{\rm Al^+}$, and (c) $n_{\rm i}=n_{\rm Al^{2+}}$ for the discharge with the Al target, and for voltages $U_{\rm D}$ in

the range from 360 V to 1000 V. Here n_n is the neutral density for the species investigated and $\sum n_{\mathrm{i},i}$ is the sum over all ions of that species. For the discharge with Ti target the corresponding fractions are shown in Figure 6 for the different magnetic field strengths and frequencies studied.

For the discharge with Al target, it is seen in Figure 5 (a) that the degree of Ar ionization is always well below 10 %. For low discharge voltages it follows rather well the time-evolution of the discharge current. For higher discharge voltages the degree of Ar ionization, except for a short initial peak, decreases with increased discharge voltage. In an earlier study [8, Fig. 5(b)] we saw that although the discharge current increased with increased discharge voltage (and here we see in figure 5 (d) that n_e increases), the electron temperature T_e decreases substantially. This explains how there can be a decreasing ionization efficiency of Ar with increasing discharge voltage. For higher discharge voltages the first peak is, however, higher than the following plateau value and the initial ionization peak value is highest for the highest discharge voltage of 1000 V. This result is connected to an initial burst of hot electrons, also seen experimentally [58, 59], which effectively ionizes the argon working gas during the initial stage of the discharge pulse. In the case of the discharges with Ti target, the degree of Ar ionization reaches at most 18 % for the highest peak current, Figure 6 (a). Here, the degree of argon ionization always follows the trend of the current evolution.

The degree of ionization for the sputtered metal is considerably higher for the singly charged metal ions compared to the argon ions, see Figure 5 (b) for the Al^+ ionization fraction and Figure 6 (d), (e) and (f) for the Ti^+ ionization fraction, and reaches about 60 % for the highest peak currents in both cases. The temporal behavior of these ion fractions follows rather well the discharge current evolution, as expected, since a large fraction of the current is carried by the singly charged metal ions. For increasing discharge voltage, we see in Figure 5 (b) that the ionization degree of Al^+ increases as the ionization degree of Ar^+ decreases along with decreasing electron temperature T_e. With this shift in the ion composition the total ion density increases as seen in the increasing electron density with increasing discharge voltage as seen in Figure 5 (d). In fact, the electron density for a discharge with Al target shown in Figure 5 (d) follows closely the discharge current shown in Figure 3. For the Ti target the degree of Ti ionization stays pretty high during the entire pulse, but decreases for decreasing magnetic field strength $|\mathbf{B}|$. Notice that the degree of of Ti ionization even increases at pulse-off for the strongest magnetic field BF1 and BF2,

as seen in Figures 4 (d), (e) and (f). The explanation is that for these cases the discharge voltage U_D drops to zero well before the pulse-end, as seen in Figures 4 (a), (d) and (g), and thereby kills off the sputtering and thus the production of neutral Ti. The remaining Ti^+ will thereby constitute a large fraction compared to the small Ti neutral density. Another way of seeing that the ion densities are low is to look at the electron densities in Figures 6 (j), (k) and (l), which are very low at pulse-off ($t > 100\mu s$) for all cases investigated.

Concerning the twice ionized metal the situation is quite different between the discharges with Al and Ti targets. In the case of Al, the ionization degree of Al^{2+}, seen in Figure 5 (c), shows that Al^{2+} only plays a minor role, since it never reaches more than about 1 % ionization fraction. It also means that the secondary electron emission due to aluminum ion bombardment is negligible, since singly charged Al^+-ions have a secondary electron emission yield close to zero and very few Al^{2+}-ions are present. However, for Ti, the ionization degree of Ti^{2+} is about one third of the ionization degree of Ti^+, as shown in Figures 6 (d), (e) and (f) and Figures 6 (g), (h) and (i), respectively. Note that the second ionization energy of Ti is 13.58 eV, or significantly lower than the second ionization energy of Al, which is 18.8 eV, while the first ionization energy of argon is 15.76 eV. Thus we would expect a much higher density of Ti^{2+} when operating with a Ti target than that of Al^{2+} while operating with an Al target. We see this more clearly in Figure 7 where we explore the discharge current composition for the discharge with Al target at 400 V and 800 V discharge voltage. When the discharge is operated at 400 V the contributions of Al^+ and Ar^+-ions to the discharge current are very similar, while the contributions from Al^{2+}-ions and secondary electrons are much smaller. At 800 V Al^+-ions dominate the discharge current while the contribution of Ar^+ is below 10 % except at the initiation of the pulse, and Al^{2+}-ions and secondary electrons have much smaller contribution. The discharge current composition for a discharge with Ti target is shown in Figure 8. The largest contribution is from Ar^+-ions while the contribution of Ti^+-ions is somewhat smaller and Ti^{2+}-ions have even smaller contribution. The contribution of Ar^+ and the sum of the contributions of Ti^+ and Ti^{2+} are of similar magnitude. This is consistent with experimental findings that HIPIMS discharges with Ti target can produce significant amounts of multiply charged titanium ions [60, 61]. Bohlmark et al. [60] claim that while sputtering a Ti target in Ar discharge up to 24 % of the ion flux consists of Ti^{2+}. However, while sputtering an Al target in Ar/N_2 mixture Jouan et al. [62] detect Al^{2+} but its intensity is orders of magnitude lower than Al^+.

Further evidence of the differences between the discharges with Al and Ti target are found when comparing the fraction of the Ohmic heating [7, 63] in Figure 5 (e) (for the Al target) and Figures 6 (m), (n) and (o) (for the Ti target) with the twice ionized metal fractions in Figure 5 (c) (Al) and Figures 6 (g), (h) and (i) (Ti). For the Al target, the fraction of the total electron heating that is attributable to Ohmic heating is found in the range of 0.87 (360 V) to 0.99 (1000 V). This particular result has previously been discussed by Huo et al. [7], where we show that with a HiPIMS discharge with Al target operated at typical high discharge voltages, almost all of the electron-heating is of Ohmic nature and located within the IR as shown in Figure 5 (e). The energetic secondary electrons accelerated in the cathode sheath, as well as the twice ionized Al^{2+} play small roles. For the discharge with Ti target, we instead find a mix of Ohmic heating and sheath energization, which is a result both of the presence of more Ar^{+}-ions, and of the ionization degree of Ti^{2+} being at least ten times larger than the ionization degree of Al^{2+}. In the Ti target case, the fraction of the total electron heating that is attributable to Ohmic heating is about 0.92 as seen in Figure 6 (m), (n) and (o). These figures also show that decreasing the magnetic field strength (BF1 to BF4) slightly reduces the Ohmic heating fraction for 100 and 150 Hz pulse frequency. For 75 Hz pulse frequency the Ohmic heating fraction initially decreases with decreasing magnetic field strength but then increases with decreasing magnetic field strength towards the end of the pulse. We will return to the physics behind the observed changes in the Ohmic heating fraction in section VI B.

The difference between the two discharges as surveyed above can be understood within the framework of generalized recycling [11, 25]. The discharge is in this description characterized by the relative fractions of three types of ion currents at the target surface. A primary current $I_{\rm prim}$ is defined as ions of the working gas, here Ar^{+}, that are ionized for the first time and then drawn to the target. This is the dominating current in dc magnetron sputtering discharges but, as Huo et al. [8] showed, the maximum steady state supply rate of atoms from the surrounding gas reservoir gives a critical upper limit to how large $I_{\rm prim}$ can become, in practical units

$$I_{\rm crit} = K_{\rm crit} S_{\rm target} p_{\rm g} \tag{27}$$

where the constant is $K_{\rm crit} \approx 0.2$ for argon gas at room temperature, $p_{\rm g}$ is the gas pressure in Pa, and $S_{\rm target}$ is the target surface area in cm^2. Discharge currents $I_{\rm D}$ above $I_{\rm crit}$ are only

possible if there is some kind of recycling of atoms that leave the target, become subsequently ionized and then are drawn back to the target. Such atoms can either be of the sputtered material which gives a self-sputter recycling current $I_{\mathrm{SS-recycle}}$, or neutralized and returning working gas atoms which gives a gas-recycling current $I_{\mathrm{gas-recycle}}$ [11].

The separate treatment of the two returning Ar^{H} and Ar^{W} populations in the IRM allows us to characterize the studied discharges with respect to the contributions of these three current types. For the Al target discussed here the critical current from Eq. (27) is $I_{\mathrm{crit}} = 7$ A. Figure 3 shows that the experiment is operated from far below I_{crit} to high above it, up to 36 A. The trend with increasing current above I_{crit} is that I_{prim} gradually becomes a very small fraction of the discharge current I_{D}, which instead becomes mainly carried by singly charged Al^{+} ions, meaning that the current $I_{\mathrm{SS-recycle}}$ dominates. Also the energy balance changes character at high currents. The domination of Al^{+}-ions, which have zero secondary electron emission yield, has the consequence that there is negligible sheath energization. The energy balance in the discharge therefore becomes dominated by Ohmic heating. Let us call this discharge "type A", and by contrast define the other extreme as "type B": a hypothetical discharge with little SS-recycling and significant working gas-recycling, and with little Ohmic heating and significant sheath energization. With this classification we can identify the discharge with Al target as an almost pure "type A" discharge.

Also the discharges with the Ti target is operated with peak current far above the critical current (up to 650 A, while $I_{\mathrm{crit}} = 19$ A). However, this discharge shows close to a 50/50 combination of self-sputter recycling $I_{\mathrm{SS-recycle}}$ and working gas-recycling $I_{\mathrm{gas-recycle}}$. As regard to the energy balance, almost 2/3 of the current to the target is here carried by Ar^{+} and Ti^{2+}-ions, see Figure 8, which both can emit secondary electrons upon target bombardment, and this gives a significant sheath energization. These two observations hold for the whole range of studied $|\mathbf{B}|$-field strengths. The discharge with Ti target can be classified as "type AB", somewhere mid-between type A and type B.

The question is why a discharge with currents above I_{crit} goes in one or the other direction in the range from type A to type B, in particular how it depends on the gas pressure, how it scales with the size of the target, and how it is influenced by the atomic and material properties of the target material. Here we can make the following observations:

- The difference in pressure (1.8 Pa and 0.54 Pa) influences the critical current according to Eq. (27). Since both discharges are operated far above I_{crit} they are therefore forced

into some type of recycling, but the pressure difference does not directly favor type A or type B.

- The larger linear size, by a factor of three, of the Ti target gives a larger extent of the ionization region perpendicular to the target. This increases the probability for returning Ar atoms from the target to become ionized and back-attracted during their transit through the IR which favors $I_{\mathrm{gas-recycle}}$ and should push the Ti target discharge towards type B as observed.

- The self-sputter yield is $Y_{\mathrm{SS}} = 1.6$ for Al^{+}-ions at 1000 eV energy which makes self-sputter recycling easy, and favors type A. By contrast $Y_{\mathrm{SS}} = 0.5$ for Ti^{+}-ions at 400 – 600 eV energy (the discharge voltage at current maximum which depends on the $|\mathbf{B}|$-field strength). This disfavors $I_{\mathrm{SS-recycle}}$ and therefore should push the Ti target discharge towards type B as observed.

- The ionization threshold for twice ionized Al^{2+}, 18.8 eV, is so high that few such ions are produced, and thus as a consequence very few secondary electrons are generated by Al^{2+}. This acts in a direction of a "low-energy" EEDF, which in turn reduces the rate of Ar ionization, reduces $I_{\mathrm{gas-recycle}}$, and therefore should push the discharge with the Al target towards type A as observed. The situation is reversed for the discharge with Ti target, where the ionization threshold for creating Ti^{2+} is much lower, 13.58 eV, and thus should push the discharge towards type B as observed.

In summary, we can conclude that there are several separate reasons for the observed differences between the discharges investigated, and that all of them (which might be circumstantial) act so as to give the observed difference. The most important aspect, however, is proposed to be the difference in self-sputter yield.

B. The effect of varying B-field strength

For the discharges with a Ti target, we see the contributions to the discharge current for two cases, weak and strong magnetic field, at 75 Hz pulse frequency, in Figure 8. We see that a stronger magnetic field leads to a higher discharge current, see also Figure 4. The higher magnetic field strength is correlated to more efficient ionization, such that the

electron density reaches the highest peak value at 75 Hz for the strongest magnetic field. The electron density peak decreases with decreasing magnetic field strength and increasing pulse frequency. We also note that a higher magnetic field strength leads to higher relative contribution of Ti^{2+} to the discharge current while it lowers the relative contribution of Ti^{+}.

Figures 6 (a) – (i) all show that a lower magnetic field strength $|\mathbf{B}|$ gives a lower degree of ionization for argon atoms, metal atoms, and metal ions. Since neutral atoms are not back-attracted, this could also increase the deposition rate. In fact Mishra et al. [54] report that a 33 % reduction in the magnetic field strength increases the deposition rate by a factor of 6 at a typical position of the substrate (100 mm from the titanium target). Also Čapek et al. [64] report a significant increase in the deposition rate with lowered magnetic field strength while depositing Nb thin films by HiPIMS. This is consistent with results obtained by Bradley et al. [56], who showed that the product of the probability of ionization and back-attraction to the target, $\alpha\beta$, decreases with decreasing $|\mathbf{B}|$ strength. This corresponds to higher ionic fluxes and higher deposition rates at the substrate $\propto (1-\alpha\beta)$. However, for these two factors, only the decrease of α can be verified by our model runs (see [8, fig. 5 (a)]), since the results in the present work is under the precondition that β is a fixed value at different pulse frequencies and magnetic field strength. However, β is uncertain since the current fits can be made within a range of β values, as explored in a previous work [5].

The standard wisdom regarding the role of the magnetic field in sputtering magnetrons is that it confines the high energy electrons that have been accelerated across the sheath, and that therefore resulting in their energy is used for ionization rather than being lost from the discharge. In this picture, a reduction of the magnetic field gives a less efficient discharge due to a loss of energetic electron confinement, less ionization, and a lower current at a given input power. The effect of changing the $|\mathbf{B}|$-field strength is here studied only for the discharge with a Ti target, and in a first look the results appear to support this explanation. As can be seen in figure 4 the reduction of $|\mathbf{B}|$ from its nominal value results in a decrease of the current while the voltage increases. The effective discharge resistance ($R_{\mathrm{D}} = U_{\mathrm{D}}(I_{\mathrm{Dmax}})/I_{\mathrm{Dmax}}$) evaluated at the time of current maximum) is plotted in Figure 9. As can be seen it decreases by a factor of 3 when the B field is increased by a factor of two. The problem is that it is hard to motivate this large change by a variation in electron confinement. Also for the weaker $|\mathbf{B}|$-field the energetic electrons are well confined in the sense that their gyro radius (of the order of mm) is much smaller than the extent of the

ionization region (of the order of cm). An alternative/additional explanation is needed.

This problem can now be resolved through an argument in two steps. The first step is that the IRM shows that a stronger magnetic field gives a higher voltage fraction across the IR. The IRM fitting parameter $f = U_{\rm IR}/U_{\rm D}$ shows the trend, and is drawn by a solid line in Figure 9 from BF1 to BF4. A dashed line furthermore illustrates that this trend in f is consistent with a gradual transition, when $|\mathbf{B}|$ is lowered, towards an ordinary glow discharge that is characterized by zero $|\mathbf{B}|$-field and with at most a few volts across the presheath. The second step in the argument is that, through the mechanism of Ohmic heating, a magnetic field adds the possibility of electron energization outside the sheath where it is more efficient than sheath energization (in the sheath typically 90 % of the energy goes to the ions, and is lost to heating the target). To see this more clearly, we first write the secondary electron current in the sheath as $I_{\rm e,SH} = \left(I_{\rm Ar^+}\gamma_{\rm Ar^+} + \frac{1}{2}I_{\rm M^{2+}}\gamma_{\rm M^{2+}}\right)(1-r)m$ and the Ohmic heating power that goes to the cold electron population in the IR as $P_{\rm Ohm} \approx I_{\rm D}U_{\rm IR}/2$ then Eq. (20) can be rewritten as

$$P_{\rm e} = P_{\rm e,SH} + P_{\rm e,IR} = I_{\rm e,SH}\left(U_{\rm D} - U_{\rm IR}\right) + \frac{I_{\rm D}U_{\rm IR}}{2} \tag{28}$$

which is the total power that goes to electron energization obtained by Huo et al. [7]. We can write the electron current in the sheath as $I_{\rm e,SH} \sim \gamma_{\rm SE}m(1-r)I_{\rm D} \sim 0.05I_{\rm D}$ and based on previous assumption the electron current in the IR is $I_{\rm e,IR} \sim 0.5 \times I_{\rm D}$. Thus Ohmic heating is more efficient due to $I_{\rm e,SH} \ll I_{\rm D}/2$. This increases the ionization rate for a given power input, and therefore gives a higher current at a lower voltage. This is by definition a lower discharge impedance – precisely the trend seen in Figure 9.

VII. CONCLUSIONS

The IRM is a time-dependent plasma discharge model and has been under continuous development during the past seven years. We discuss and summarize the development of the IRM and apply it to explore argon discharge with both Al and Ti target. In the present work, we give a complete description of the most recent version of the IRM, which includes improvements, such as allowing for returning of the working gas atoms from the target, a separate treatment of hot secondary electrons, and addition of doubly charged metal ions.

To show the general applicability of the IRM, two different HiPIMS discharges were investigated. The first set concerns 400 μs long discharge pulses applied to an Al target in an Ar atmosphere at 1.8 Pa and the other has to do with a 100 μs long discharge pulses to a Ti target in an Ar atmosphere at 0.54 Pa. The electron density follows the discharge current for discharge with both Al and Ti target. We find that there is a significant density of Ti^{2+}-ions when operating with a Ti target while the density of Al^{2+}-ions is low when operating with Al target. We find that Al^{2+}-ions contribute negligibly to the production of secondary electrons, while Ti^{2+}-ions effectively contribute to the production of secondary electrons. The model results show that for the argon discharge with Al target the contribution of Al^{+}-ions to the discharge current is over 90 % at 800 V, while Al^{+}-ions and Ar^{+}-ions contribute roughly equally to the discharge current at 400 V. Thus for high currents the discharge with Al target develops almost pure self-sputter recycling, while the discharge with Ti target exhibits close to a 50/50 combination of self-sputter recycling and process gas-recycling. The reason is shown to be that, for Ti target, a self-sputter yield significantly below unity makes gas-recycling necessary at high currents.

For the Ti target we explored the effects when varying the magnetic field strength. The electron density decreases with increasing pulse frequency and decreasing magnetic field strength. We also demonstrate how the magnetic field strength influences the discharge current and its composition when operating with Ti target and find that stronger magnetic field increases the relative contribution of Ti^{2+}-ions to the discharge current. We find that for a discharge with a titanium target the ionization fractions for Ar^{+}-ions, Ti^{+}-ions and Ti^{2+}-ions decrease with increased magnetic field strength. The ionization fractions for Ar^{+}-ions, and Ti^{2+}-ions decrease with increased pulse frequency. In the discharge with Ti target the **B**-field was reduced in steps from the nominal value, which resulted in a corresponding stepwise increase in the discharge resistivity.

Acknowledgments

J. T. G and N. B. gratefully acknowledge the hospitality of CNRS and University Paris-Sud, Orsay where much of this study was made. This work was partially supported by the Icelandic Research Fund Grant No. 130029, the Swedish Government Agency for Innovation

Systems (VINNOVA) contract no. 2014-04876.

---

[1] U. Helmersson, M. Lattemann, J. Bohlmark, A. P. Ehiasarian, and J. T. Gudmundsson, Thin Solid Films **513**, 1 (2006).

[2] J. T. Gudmundsson, N. Brenning, D. Lundin, and U. Helmersson, Journal of Vacuum Science and Technology A **30**, 030801 (2012).

[3] D. Lundin and K. Sarakinos, Journal of Materials Research **27**, 780 (2012).

[4] M. A. Raadu, I. Axnäs, J. T. Gudmundsson, C. Huo, and N. Brenning, Plasma Sources Science and Technology **20**, 065007 (2011).

[5] C. Huo, M. A. Raadu, D. Lundin, J. T. Gudmundsson, A. Anders, and N. Brenning, Plasma Sources Science and Technology **21**, 045004 (2012).

[6] N. Brenning, D. Lundin, M. A. Raadu, C. Huo, C. Vitelaru, G. D. Stancu, T. Minea, and U. Helmersson, Plasma Sources Science and Technology **21**, 025005 (2012).

[7] C. Huo, D. Lundin, M. A. Raadu, A. Anders, J. T. Gudmundsson, and N. Brenning, Plasma Sources Science and Technology **22**, 045005 (2013).

[8] C. Huo, D. Lundin, M. A. Raadu, A. Anders, J. T. Gudmundsson, and N. Brenning, Plasma Sources Science and Technology **23**, 025017 (2014).

[9] G. D. Stancu, N. Brenning, C. Vitelaru, D. Lundin, and T. Minea, Plasma Sources Science and Technology **24**, 045011 (2015).

[10] J. T. Gudmundsson, D. Lundin, G. D. Stancu, N. Brenning, and T. M. Minea, Physics of Plasmas **22**, 113508 (2015).

[11] J. T. Gudmundsson, D. Lundin, N. Brenning, M. A. Raadu, C. Huo, and T. M. Minea, Plasma Sources Science and Technology **25**, 065004 (2016).

[12] D. Lundin, J. T. Gudmundsson, N. Brenning, M. A. Raadu, and T. M. Minea, Journal of Applied Physics **121**, 171917 (2017).

[13] M. I. Hasan, I. Pilch, D. Söderström, D. Lundin, U. Helmersson, and N. Brenning, Plasma Sources Science and Technology **22**, 035006 (2013).

[14] N. Brenning, I. Axnäs, M. A. Raadu, D. Lundin, and U. Helmerson, Plasma Sources Science and Technology **17**, 045009 (2008).

[15] C. Huo, Ph.D. thesis, KTH Royal Institute of Technology, Stockholm (2013).

[16] A. Anders, J. Andersson, and A. Ehiasarian, Journal of Applied Physics **102**, 113303 (2007).

[17] A. Mishra, P. J. Kelly, and J. W. Bradley, Journal of Physics D: Applied Physics **44**, 425201 (2011).

[18] A. Hecimovic, V. Schulz-von der Gathen, M. Böke, A. von Keudell, and J. Winter, Plasma Sources Science and Technology **24**, 045005 (2015).

[19] A. Hecimovic, C. Maszl, V. Schulz-von der Gathen, M. Böke, and A. von Keudell, Plasma Sources Science and Technology **25**, 035001 (2016).

[20] A. Hecimovic, C. Corbella, C. Maszl, W. Breilmann, and A. von Keudell, Journal of Applied Physics **121**, 171915 (2017).

[21] M. Panjan and A. Anders, Journal of Applied Physics **121**, 063302 (2017).

[22] J. A. Thornton, Journal of Vacuum Science and Technology **15**, 171 (1978).

[23] G. Buyle, W. De Bosscher, D. Depla, K. Eufinger, J. Haemers, and R. De Gryse, Vacuum **70**, 29 (2003).

[24] A. Revel, T. Minea, and S. Tsikata, Physics of Plasmas **23**, 100701 (2016).

[25] A. Anders, J. Čapek, M. Hála, and L. Martinu, Journal of Physics D: Applied Physics **45**, 012003 (2012).

[26] J. T. Gudmundsson, Journal of Physics: Conference Series **100**, 082013 (2008).

[27] A. V. Phelps, C. H. Greene, and J. P. Burke, Journal of Physics B: Atomic, Molecular and Optical Physics **33**, 2965 (2000).

[28] D. W. Hoffman, Journal of Vacuum Science and Technology A **3**, 561 (1985).

[29] S. M. Rossnagel, Journal of Vacuum Science and Technology A **6**, 19 (1988).

[30] I. Kolev and A. Bogaerts, Journal of Applied Physics **104**, 093301 (2008).

[31] D. Lundin, N. Brenning, D. Jadernas, P. Larsson, E. Wallin, M. Lattemann, M. A. Raadu, and U. Helmersson, Plasma Sources Science and Technology **18**, 045008 (2009).

[32] J. W. Bradley, S. Thompson, and Y. A. Gonzalvo, Plasma Sources Science and Technology **10**, 490 (2001).

[33] A. Rauch, R. J. Mendelsberg, J. M. Sanders, and A. Anders, Journal of Applied Physics **111**, 083302 (2012).

[34] D. Depla, S. Mahieu, and R. De Gryse, Thin Solid Films **517**, 2825 (2009).

[35] R. A. Baragiola, E. V. Alonso, J. Ferron, and A. Oliva-Florio, Surface Science **90**, 240 (1979).

[36] M. A. Lieberman and A. J. Lichtenberg, *Principles of Plasma Discharges and Materials*

Processing (John Wiley & Sons, New York, 2005), 2nd ed.

[37] A. T. Hjartarson, E. G. Thorsteinsson, and J. T. Gudmundsson, Plasma Sources Science and Technology **19**, 065008 (2010).

[38] J. Lu and M. J. Kushner, Journal of Applied Physics **87**, 7198 (2000).

[39] R. S. Freund, R. C. Wetzel, R. J. Shul, and T. R. Hayes, Physical Review A **41**, 3575 (1990).

[40] S. J. T. Hayton and B. Peart, Journal of Physics B: Atomic, Molecular and Optical Physics **27**, 5331 (1994).

[41] E. J. McGuire, Physical Review A **26**, 125 (1982).

[42] C. A. Wells and K. J. Miller, Physical Review A **12**, 17 (1975).

[43] P. L. Bartlett and A. T. Stelbovics, Atomic Data and Nuclear Data Tables **86**, 235 (2004).

[44] H. Deutsch, K. Becker, and T. Märk, International Journal of Mass Spectrometry **271**, 58 (2008).

[45] M. J. Diserens, A. C. H. Smith, and M. F. A. Harrison, Journal of Physics B: Atomic, Molecular and Optical Physics **21**, 2129 (1988).

[46] R. H. Neynaber, L. L. Marino, E. W. Rothe, and S. M. Trujillo, Physical Review **129**, 2069 (1963).

[47] C. A. Ramsbottom and K. L. Bell, Physica Scripta **50**, 666 (1994).

[48] Y. Yamauchi and R. Shimizu, Japanese Journal of Applied Physics **22**, L227 (1983).

[49] W. H. Hayward and A. R. Wolter, Journal of Applied Physics **40**, 2911 (1969).

[50] D. N. Ruzic, in *Handbook of Plasma Processing Technology: Fundamentals, Etching, Deposition, and Surface Engineering*, edited by S. M. Rossnagel, W. D. Westwood, and J. J. Cuomo (Noyes Publications, Park Ridge, NJ, 1990), pp. 70–90.

[51] J. T. Gudmundsson and E. G. Thorsteinsson, Plasma Sources Science and Technology **16**, 399 (2007).

[52] M.-H. Lee and C.-W. Chung, Physics of Plasmas **12**, 073501 (2005).

[53] S. Ashida, C. Lee, and M. A. Lieberman, Journal of Vacuum Science and Technology A **13**, 2498 (1995).

[54] A. Mishra, P. J. Kelly, and J. W. Bradley, Plasma Sources Science and Technology **19**, 045014 (2010).

[55] J. W. Bradley, personal communication (2013).

[56] J. W. Bradley, A. Mishra, and P. J. Kelly, Journal of Physics D: Applied Physics **48**, 215202

(2015).

[57] D. J. Christie, Journal of Vacuum Science and Technology A **23**, 330 (2005).

[58] P. Poolcharuansin and J. W. Bradley, Plasma Sources Science and Technology **19**, 025010 (2010).

[59] A. D. Pajdarová, J. Vlček, P. Kudláček, and J. Lukáš, Plasma Sources Science and Technology **18**, 025008 (2009).

[60] J. Bohlmark, M. Lattemann, J. T. Gudmundsson, A. P. Ehiasarian, Y. A. Gonzalvo, N. Brenning, and U. Helmersson, Thin Solid Films **515**, 1522 (2006).

[61] J. Andersson, A. P. Ehiasarian, and A. Anders, Applied Physics Letters **93**, 071504 (2008).

[62] P.-Y. Jouan, L. Le Brizoual, C. Cardinaud, S. Tricot, and M. A. Djouadi, IEEE Transactions on Plasma Science **38**, 3089 (2010).

[63] N. Brenning, J. T. Gudmundsson, D. Lundin, T. Minea, M. A. Raadu, and U. Helmersson, Plasma Sources Science and Technology **25**, 065024 (2016).

[64] J. Čapek, M. Hála, O. Zabeida, J. E. Klemberg-Sapieha, and L. Martinu, Journal of Physics D: Applied Physics **46**, 205205 (2013).

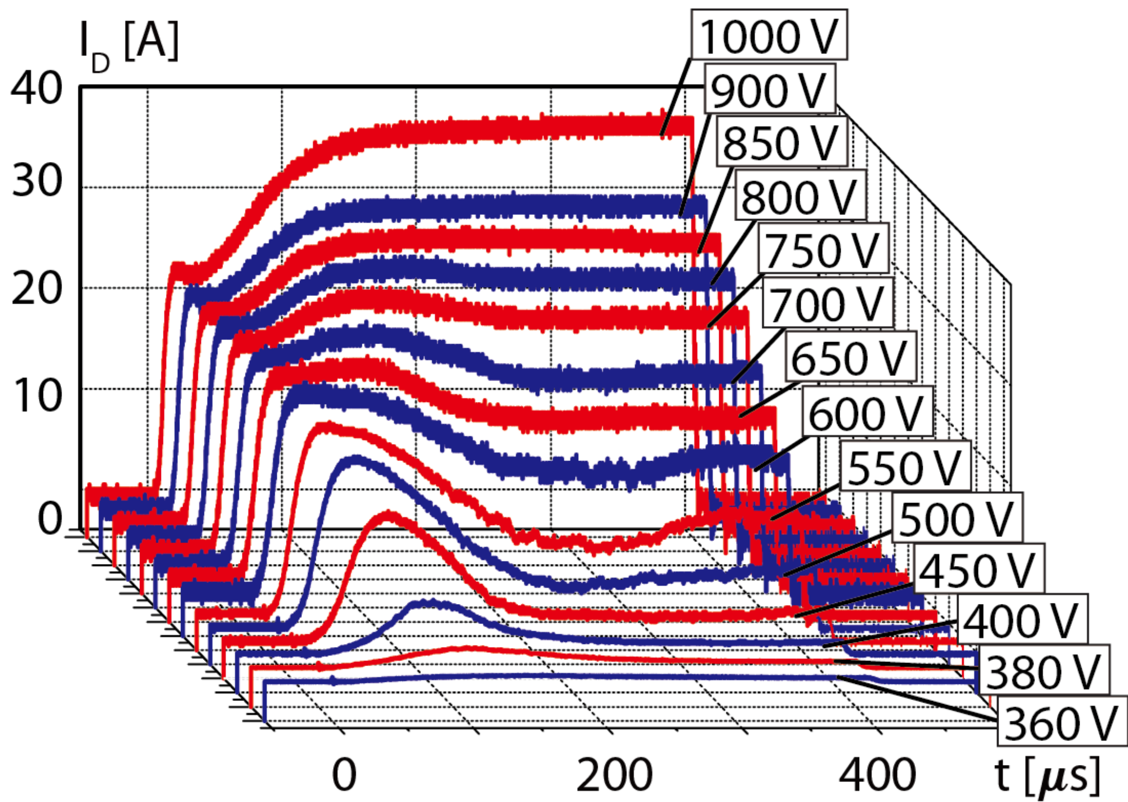

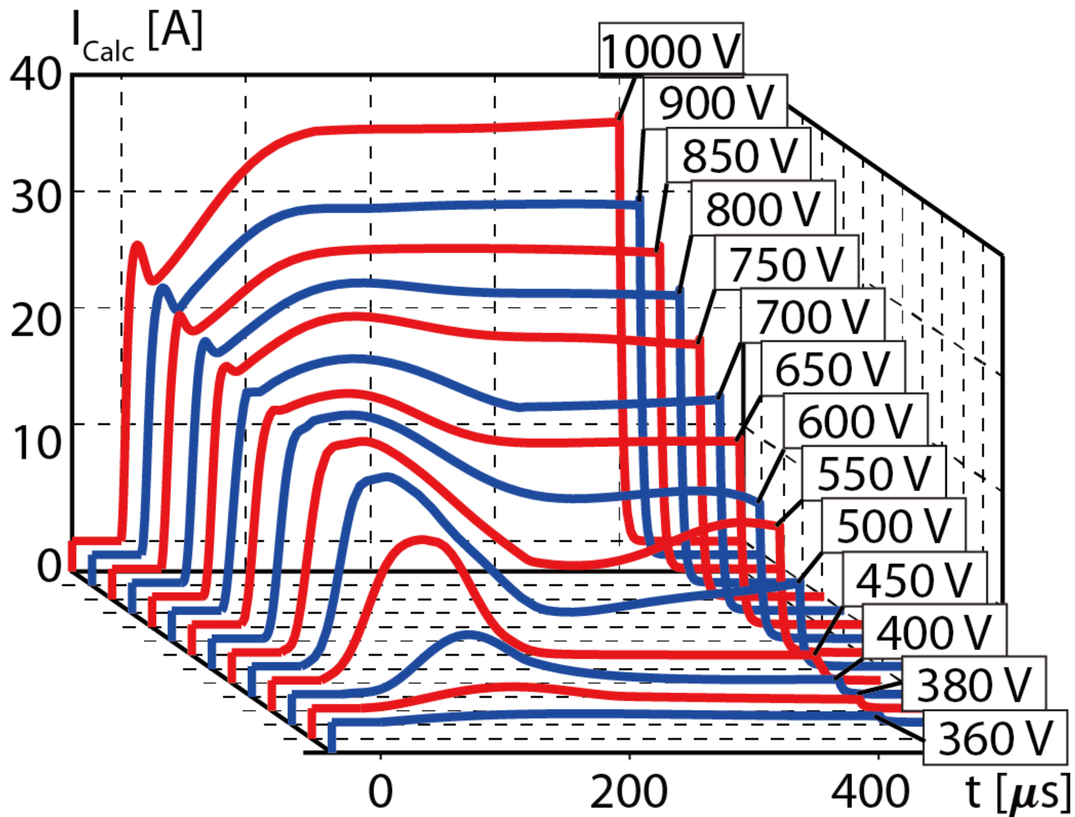

FIG. 3: (a) Experimentally determined temporal variations of the discharge current for various discharge (cathode) voltages. The target is Al 50 mm in diameter. After Anders et al. [16]. (b) The discharge currents calculated by the IRM for HiPIMS discharge with 50 mm Al target.

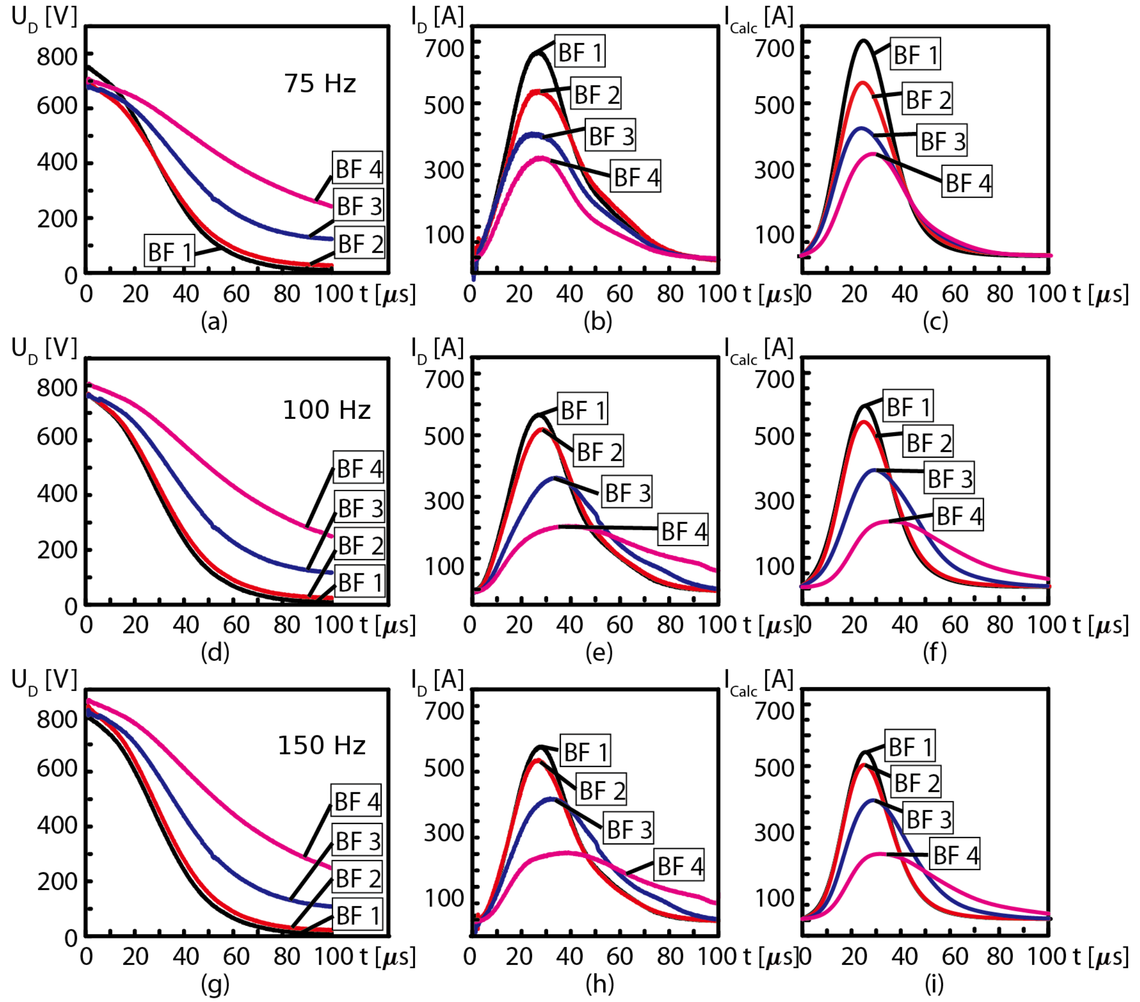

FIG. 4: Experimentally determined variation of the discharge currents for various cathode voltages at different magnetic field strengths for pulse frequencies 75 Hz, 100 Hz, and 150 Hz. The cathode target is made of Ti, 150 mm in diameter. Based on input from Mishra et al. [54–56]. For 75 Hz pulse frequency: (a) the measured discharge voltage, (b) measured discharge current, and (c) calculated discharge current. For 100 Hz pulse frequency: (d) the measured discharge voltage, (e) measured discharge current, and (f) calculated discharge current. For 150 Hz pulse frequency: (g) the measured discharge voltage, (h) measured discharge current, and (i) calculated discharge current.

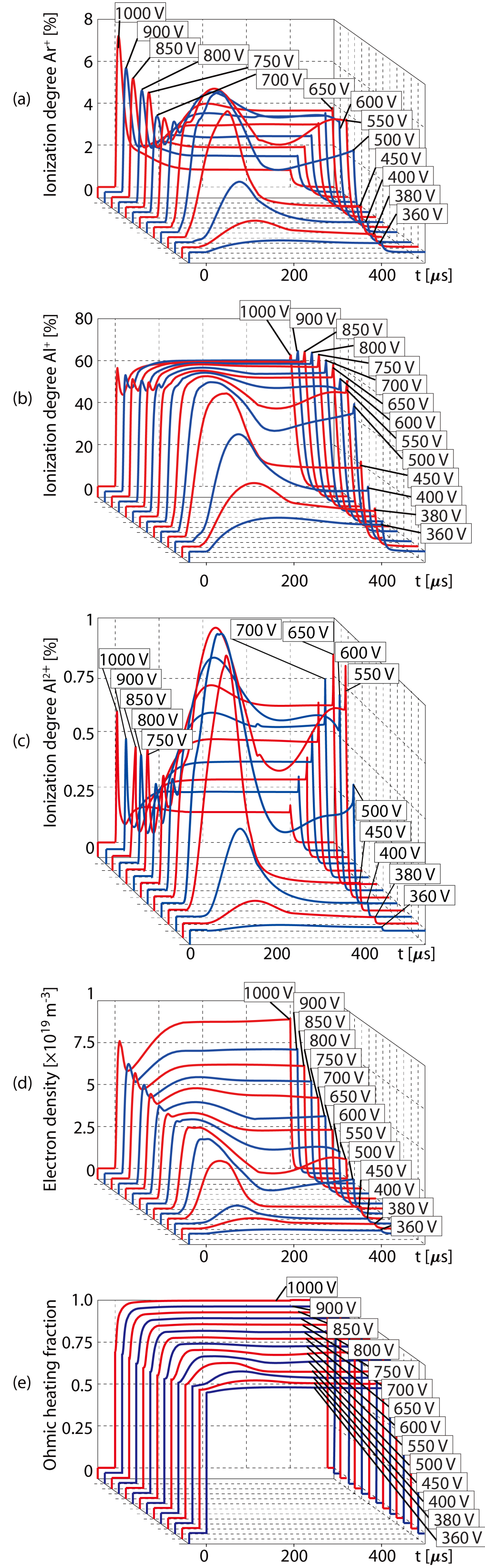

FIG. 5: The various plasma parameters for an argon discharge with Al target calculated by IRM. (a) The ionization degree of argon atoms, (b) the ionization degree of singly charged metal ions, Al^{+}, (c) the ionization degree of doubly charged metal ions, Al^{2+}, (d) the electron density, and (e) the Ohmic heating fraction

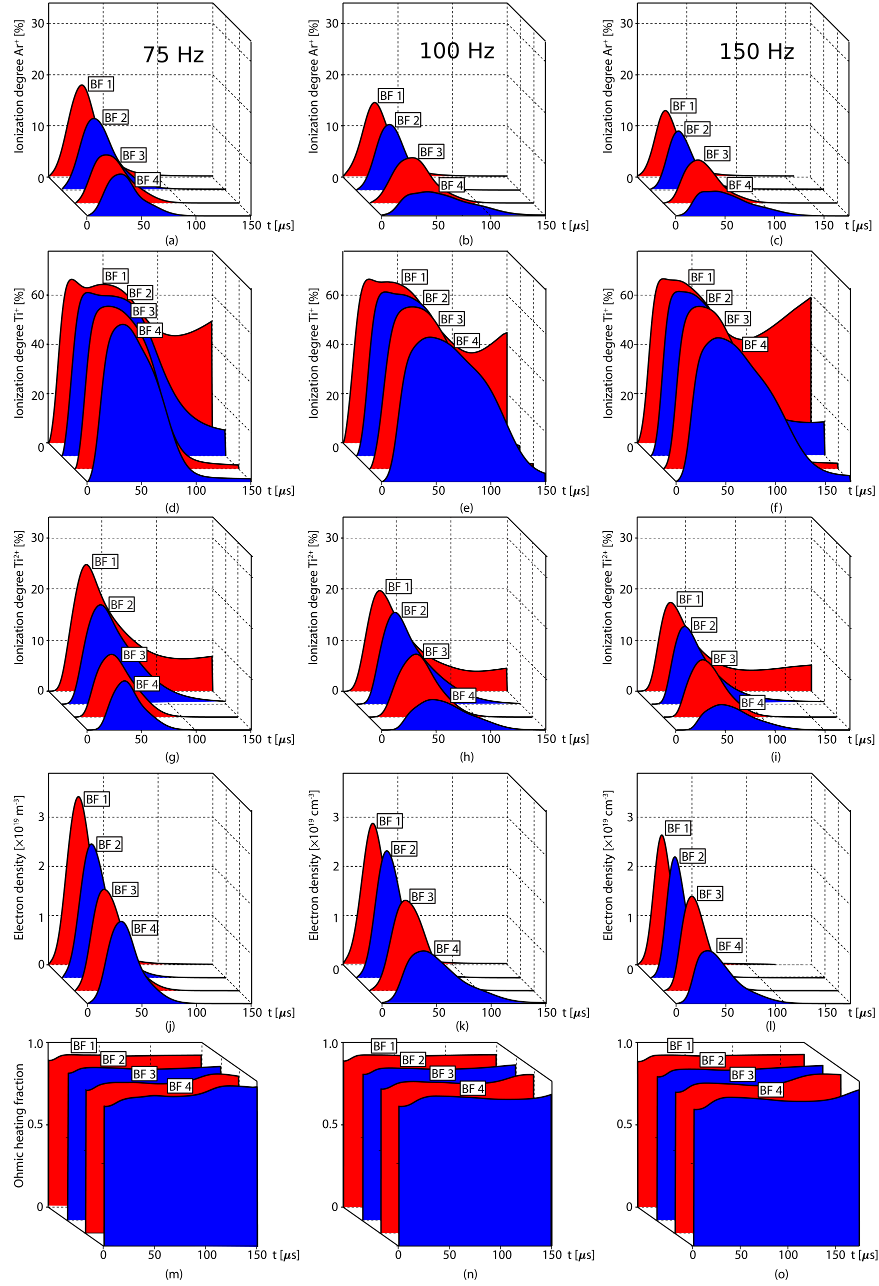

FIG. 6: The various plasma parameters for a discharge with Ti target calculated by the IRM. The ionization degree of Ar^+ for (a) 75 Hz, (b) 100 Hz, and (c) 150 Hz at different magnetic field strengths. The ionization degree of Ti^+ for (d) 75 Hz, (e) 100 Hz, and (f) 150 Hz at different magnetic field strengths. The ionization degree of Ti^{2+} for (g) 75 Hz, (h) 100 Hz, and (i) 150 Hz at different magnetic field strengths. The electron density at (j) 75 Hz, (k) 100 Hz, and (l) 150 Hz at different magnetic field strengths. Fraction of the total electron heating that is attributable to Ohmic heating at (m) 75 Hz, (n) 100 Hz, and (o) 150 Hz at different magnetic field strengths.

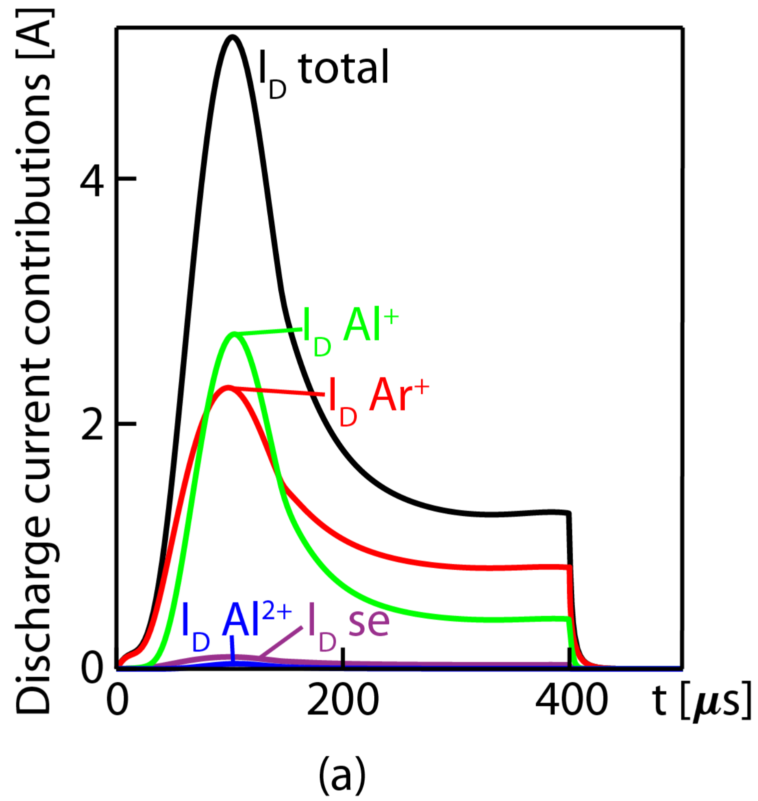

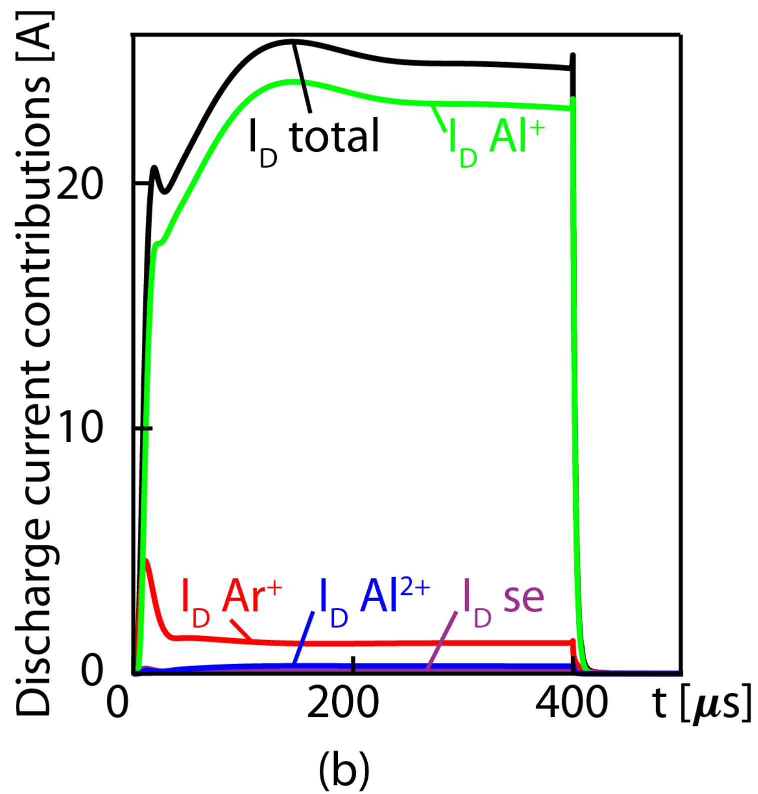

FIG. 7: The temporal variation of the discharge current composition at the target surface for an argon discharge at 1.8 Pa with 50 mm diameter Al target for discharge voltage (a) 400 V and (b) 800 V.

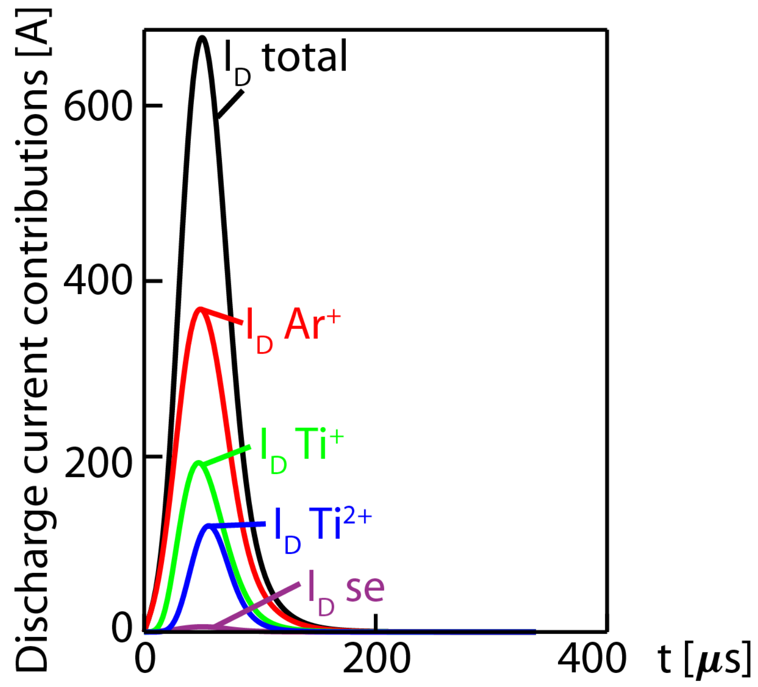

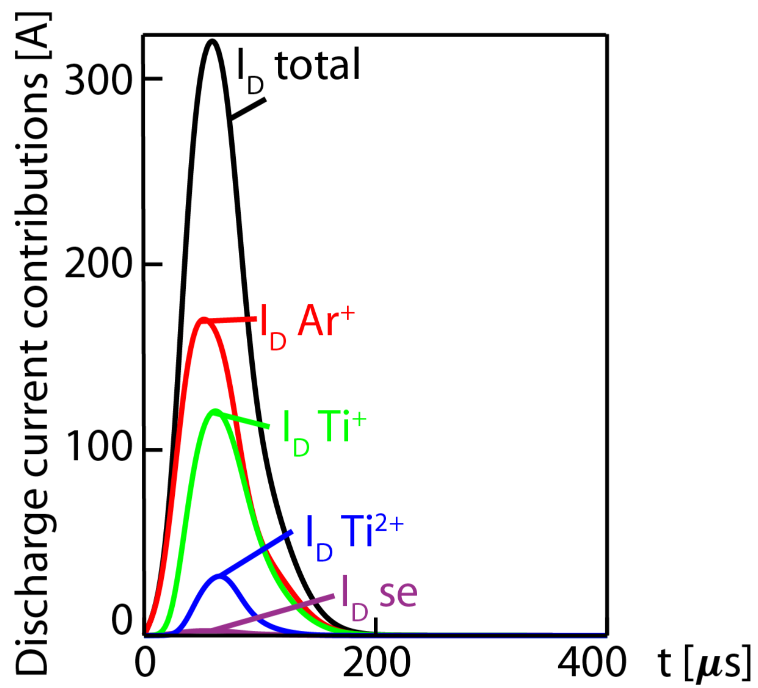

FIG. 8: The temporal variation of the discharge current composition at the target surface for an argon discharge at 0.54 Pa and pulse frequency of 75 Hz with 150 mm diameter Ti target for magnetic field strengths noted as (a) BF1 and (b) BF4.

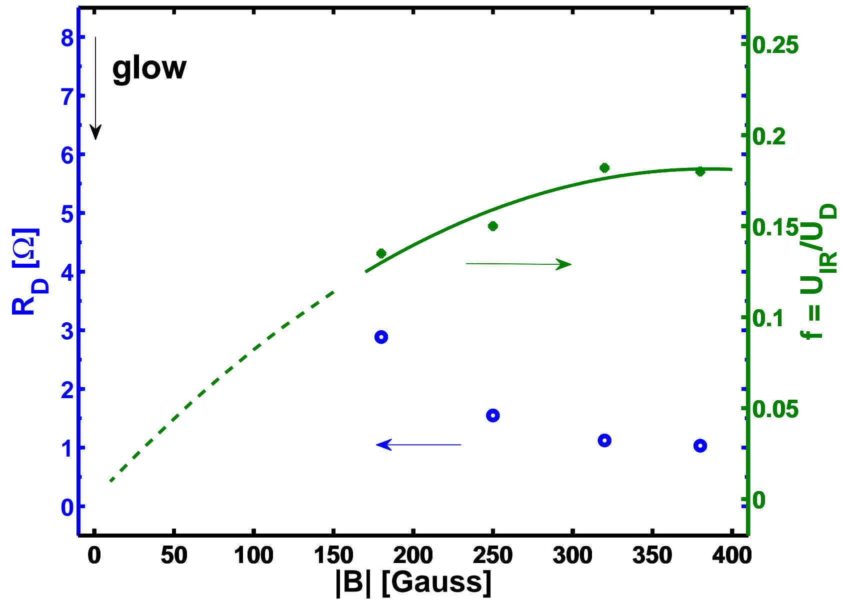

FIG. 9: The effect on the discharge physics for the discharge with Ti target operated at 100 Hz, increasing the magnetic field strength from 180 Gauss to its nominal value, 380 Gauss at the racetrack center. The effective discharge resistance $R_{\mathrm{D}} = U_{\mathrm{D}}(I_{\mathrm{Dmax}})/I_{\mathrm{Dmax}}$ at current maximum decreases, while the voltage fraction across the ionization region, $f = U_{\mathrm{IR}}/U_{\mathrm{D}}$, increases.